Master's thesis

NTNU
Norwegian University of Science and Technology
Faculty of Engineering
Department of Marine Technology

Snorre Bråthen Tjørswaag

Experimental Investigation of Dynamic Pressure Drop in a Marine Gas Injector

Master's thesis in Marine Technology
Supervisor: David Emberson
June 2022

NTNU
Norwegian University of
Science and Technology

Snorre Bråthen Tjørswaag

Experimental Investigation of Dynamic Pressure Drop in a Marine Gas Injector

Master's thesis in Marine Technology
Supervisor: David Emberson
June 2022

Norwegian University of Science and Technology
Faculty of Engineering
Department of Marine Technology

NTNU
Norwegian University of
Science and Technology

Abstract

As a consequence of stricter regulations regarding emissions and expanding emissions control areas liquefied natural gas has proven to be a viable option as an alternative fuel for the maritime shipping industry. This is due to its significant decrease in harmful and regulated emissions but also in some cases increased thermal efficiency compered with marine diesel oil engines.

Available gas engines typically fall under one of two categories, that is low or high pressure gas injection. Low pressure gas engines generally injects fuel into the intake manifold at relatively low pressures ($\leq$10 bar). However, due to very lean combustion they suffer from quenching leading to unburned methane, known as methane slip, which has a much higher global warming potential than CO_2. High pressure gas engines direct injects the gas fuel into the cylinder close to top dead center at relative high pressures of 300-350 bar. With direct injection the temperature in the cylinder can be kept higher resulting in a more complete combustion and reducing the methane slip to a minimum. However it poses it own set of challenges. . One challenge with high pressure gas injection is to maintain the pressure during the entirety of the injection. Due to the compressible nature of gasses the pressure will begin to drop as the injection starts. Meaning that the injection pressure at end of injection will be lower than the initial injection pressure. This might cause the issued jet to have different characteristics at different stages in the injection, other than the transient jet development.

This study aims to observe and quantify the influence the dynamic pressure drop has on a gas fuel injection jet. This was accomplished by injecting nitrogen into a pressurized chamber, called a constant volume combustion chamber, where the injection pressure was continuously measured and optically image the jet by applying a high speed schlieren method. The images was used to determine the cone angle and penetration length, in addition to calculate the jet tip velocity of the jet during the injection. Then the dynamic pressure drop was compered the measured characteristics from the images to determine the influence it had on the gas jet.

It turned out, in this study, that even though different injection pressures had a significant influence on the appearance of the jet, the dynamic pressure drop did not have any obvious influence.

During the development phase of the jet the associated pressure drop was less than 1% of the injection pressure, meaning that the initial conditions for the jet remained more or less

constant during this time period. When the jet had become fully developed the relative pressure drop was 5%, still there was no visible influence on the near field region of the jet related to shocks structures and the initial jet width.

Sammendrag

Som en konsekvens av strengere regulering av utslipp og utvidede utslippskontroll områder, har flytende naturgass vist å være et gunstig alternativt drivstoff for sjøfartsnæringen. Dette skyldes en betydelig reduksjonen av skadelig og regulerte utslipp, men også i noen situsjoner bedre termisk virkningsgrad.

Nåværende tilgjengelige gassmotorer faller generelt under en av to kategorier, nemlig lav- eller høytrykksinnsprøytning. Med lavtrykksinnsprøytning blir gassen ofte introdusert i innsugsmanifolden ved relativt lave trykk ($\leq$ 10 bar). På grunn av magert blandingsforhold blir forbrenningstemperaturen forholdsvis lav, som fører til ukomplett forbrenning av metan, også kjent som metan slip. Metan har et betdylig høyere globalt oppvarmingspotensial sammenlignet med CO_2 og er derfor uønsket. Med høytrykksinnsprøynting, blir gassen direkte innsprøytet inn i sylinderen, når stempelet nærmer seg øvre dødpunkt. På den måten kan temperaturen i sylinderen holdes høyere, fordi det ikke er noen risiko for banking, slik at metan slippet blir redusert til et minimum. Gassen blir typisk sprøytet inn ved et trykk på 300-350 bar. Likevel må andre utfordringer bli tatt høyde for med et slikt system.

En utfordring med høytrykks- gassinnsprøytning er at injeksjonstrykket vil falle når innsprøytningen starter, på grunn av kompressibiliteten av gasser. Dette betyr at trykket ved start- og sluttidspuktet av injeksjonen er forskjellig som kan føre til at egenskapene til gassen endrer seg under innsprøytnignen.

Målet med dette studiet er å observere og kvantifisere påvirkningen av det dynamiske trykkfallet over dysen har på utviklingen av en gass som blir innsprlytet ved høye trykk. Dette ble utført ved å injisere nitrogen inn i et trykksatt kammer, kalt et konstant-volum-forbrennings-kammer, og kontinuerlig måle trykket over dysen og optisk fotografere gassen ved hjelp av et høyhastighets schlieren oppsett. Bildene ble brukt til å beregne vinkelen og penetreringslengden av den utstedte strålen, hastigheten til strålen ble også regnet ut. Videre ble det dynamiske trykkfallet sammenlignet med de beregnede verdiene for å avgjøre i hvilken grad det påvirket strålen.

For dette eksperimentet viste deg seg at selv om det totale innsprøytningstrykket i stor grad påvirket strålen, så hadde det dynamiske trykkfallet nesten ingen påvirkning på utviklingen av den.

Gjennom utviklingsfasen av strålen var det tilhørende relative trykkfallet på under 1% av innsprøytningstrykket. Hvilket betyr at initialbetingelsene til strålen forble mer eller

mindre konstant i denne tidsperioden. Når strålen hadde blitt fult utviklet, var det relative trykkfallet på 5%, likevel var det ingen tydelig endreing i nærfeltsområdet med tanke på sjokkstrukturer og bredden for den delen av den.

Preface

This thesis is the final submission to fulfill the requirements of a master's degree in marine engineering at the Department of Marine Technology (IMT), NTNU.

The topic of the work, was selected based on a desire to practically investigate the possibilities of alternative fuels for the maritime shipping industry.

The experiments were conducted in the machinery laboratory at the Department of Marine Technology, NTNU, Trondheim during the spring of 2022, under supervision of Associate Professor David Emberson.

Snorre Bråthen Tjørswaag Date

Acknowledgements

I want to extend my sincerest gratitude to Øystein Kristiansen, now former chief engineer at NTNU. Without him, not a single aspect of this thesis would have been accomplished. Throughout the Autumn of 2021 and the spring of 2022, Øystein has been vital in order to get the combustion rig to an operational condition. In addition, he has taught me a lot in terms of having a systematic, analytical and logical approach to troubleshooting, in addition to gaining an understanding of complex systems.

Likewise, I would like to thank David Emberson for being my supervisor and his guidance and constructive criticism, which has been invaluable during the course of the work. He has taught me the importance of being goal-oriented and has been a key contributor to progress.

I would also like to thank Professor Eilif Pedersen, who took the time to answer my questions and clarify concepts. In addition to, Gisle Haugseth and Kristian Minde, both staff engineers at IMT, for sorting out technical problems for me.

Last but not least I want to thank my office mates for keeping up the morale and the for good laughs.

Contents

List of Figures

List of Tables

Nomenclature

Abbreviations

ASOI	After start of injection
BOG	Boil-off gas
BOS	Background oriented schlieren
CI	Compression Ignition
CVCC	Constant Volume Combustion Chamber
ECA	Emission control area
EGR	Exhaust Gas Recirculation
EOI	End of injection
GHG	Green house gases
HPDF	High pressure dual fuel
IMO	International Maritime Organization
LBSI	Lean burn spark ignited
LNG	Liquefied natural gas
LPDF	Low pressure dual fuel
MA	Moving average
MDO	Marine diesel oil
MGO	Marine Gas Oil
NG	Natural gas
NPR	Nozzle pressure ratio
PI	Port injection
PM	Particulate matter

SCR	Selective catalytic reduction
SOI	Start of injection
TDC	Top Dead Center
UN	United Nations

Greek symbols

δ t	Time step	[ms]
κ	Specific heat ratio	[–]
λ	Air excess ratio	[–]
σ_p	Standard deviation	[bar]
τ	Compressibility factor	$[\mathrm{m^2\,N}]$
θ	Cone angle	[°]
ρ	Density	$[\mathrm{kg\,m^{-3}}]$

Latin symbols

$\bar{R}$	Universal gas constant	$[\mathrm{kJ/kmol \cdot K}]$
A	Cross-sectional area	$[\mathrm{m^2}]$
a	Speed of sound	$[\mathrm{m\,s^{-1}}]$
F	Force	[N]
k	Gladstone-Dale constant	$[\mathrm{m^3\,kg}]$
M	Mach number	[–]
n	Refractive index	[–]
p	Pressure	[bar]
p^*	Critical pressure	[bar]
p_b	Back pressure	[bar]
$p_{drop,rel}$	Relative pressure drop	[–]
p_{drop}	Pressure drop	[bar]
p_e	Nozzle exit pressure	[bar]
p_{inj}	Injection pressure	[bar]
p_{ins}	Instantaneous pressure drop	[bar]

t	Time	[ms]
t_{asoi}	Time after start of injection	[ms]
u	Velocity	$[\mathrm{m\,s^{-1}}]$
u_{tip}	Jet tip penetration velocity	$[\mathrm{m\,s^{-1}}]$

Chapter 1

Introduction

Over 80% of the world wide trade and 70% of the corresponding value is transported by the international shipping fleet (United Nations, 2022). However, only 2.89% of the global anthropogenic green house gases (GHG) constitutes from the shipping industry (IMO, 2022). Still the shipping industry is of interest in regards to reduction of emissions and pollutants, as it faces a future of stricter regulations and sanctions in order to accommodate future restrictions. Considering that the international fleet is expected to grow in combination with an increased demand for the trade of goods, meeting these regulations pose a number of challenges. Moreover, local emissions such as particulate matter (PM), SO_x and NO_x, is a large problem in cities with large and busy ports, as they are a significant risk to human health and the local environment (Corbett et al., 2007) (Yau et al., 2013).

1.1 Motivation

Lately, emissions of greenhouse gases have attracted even more attention following the Paris Agreement and the United Nations (UN) prominent presence in the global search for reduced emissions. Although the shipping industry accounts for only a modest share of global emissions, this share may increase significantly in combination with an increase in worldwide trade. Hence, the industry is under pressure to develop more energy-efficient solutions and measures to reduce the amount of emitted greenhouse gasses and other harmful emissions. Furthermore, stricter and expanding emission control areas are an additional driving force to phase out heavy fuel oils with lighter carbon- and carbon-free fuels.

The short sea shipping segment, such as ferries and fishing vessels, may adapt to future regulations by operating with batteries and other electric power solutions. While the deep sea segment, for the foreseeable future, will continue to use a reciprocating engine as the prime mover, where the fuel gets injected and burned. Ships that sail most of the time at a constant speed and optimal engine load will be more efficient with a direct drive propulsion configuration than a diesel-electric or hybrid power system. The transmission losses in diesel-electric and hybrid power systems make direct drive configurations more

energy efficient. Secondly, due to the vast distances deep-sea ships sail, the current size of battery packs is not sufficient to power these ships.

Among the proposed solutions, liquefied natural gas (LNG) has attracted much attention in recent decades as a potential alternative fuel. Implementation of LNG as a fuel provides several advantages concerning emissions and, in some cases, thermal efficiency. Even though LNG gets stored in a liquid form, it gets injected into the cylinder as a gas. Consequently, the injection system is vastly different from a liquid fuel injection system. As the state of the fuels is different, the behavior of the fluids also varies.

The behavior of gas jets in combination with the properties of LNG has led to three qualitatively different engine designs and injection systems. Two operate with injections of relatively low pressure, in the range of 10 bar and lower, while the third exceed pressures of 300 bar. (Woodyard, 2004) (Stenersen and Thonstad, 2017).

1.2 Emissions of Concern

Carbon dioxide is often perceived as the principal culprit of greenhouse gasses and emissions because of the amount emitted. Other emissions of concern regarding greenhouse gasses include methane, CH_4, and nitrogen oxides, NO_X. Although the amount emitted by the latter two is significantly lower than CO2, their global warming potential is substantially larger. Additionally, nitrogen and sulfur oxides, SO_X, are directly correlated with acidification, typically in the form of acid rain.

The environmental impact caused by acidification led to a considerable effort to reduce the amount of emitted SO_X in the 1990s (Vestreng et al., 2007). The primary source of anthropogenic SO_X emissions is associated with the sulfur content in fossil fuels (Vestreng et al., 2007). Meaning that there are only two possible ways to reduce the amount of emitted SO_X. Either by reducing the sulfur content of the fuel or installing exhaust after-treatment systems. However, the amount of NO_X created primarily depends on the temperature during combustion, where a higher peak combustion temperature causes a significant increase in NO_X.

In addition, emissions of concern regarding shipping and compression ignition (CI) engines are called particulate matter (PM). PM is a collective term for all solid and liquid particles suspended in the air. Concerning CI engines PMs are principally composed of soot, of which organic compounds during the combustion and in the exhaust have been absorbed (Heywood, 2018). The biggest particulates have a diameter of just 10 nm and can get as small as 100 μm. Due to the fact they are suspended in air and their small size, PMs can enter the lungs of humans and from there proceed further into the bloodstream (Nelin et al., 2012). The harmful impact PM has on human health has been well documented Corbett et al. (2007) Nelin et al. (2012) and is estimated to account for approximately 60000 cardiopulmonary and lung cancer deaths annually (Corbett et al., 2007)

1.3 Liquefied Natural Gas

LNG consists of a condensed mixture of lighter hydrocarbons but is typically composed of methane and small amounts of ethane and nitrogen. Though the composition varies slightly, methane amounts to approximately 87 mol % - 98 mol %, dependent on the gas processing and given requirements and specifications. Liquefied NG has a density over 600 times as large as gaseous NG. Hence the liquefaction of the gas is done for transportation purposes. In situations where the distance between the production facility of natural gas and the consumer is greater than approximately 4000 km, natural gas transportation as LNG is a more economically viable solution than transportation in pipelines. At atmospheric pressure, LNG has a temperature of about -162 °C, slightly below the boiling temperature of pure methane. Therefore it is also a cryogenic liquid.

1.3.1 LNG as Marine Fuel

Typical LNG tankers transport LNG at atmospheric pressure close to the vaporization temperature, at approximately -163 °C. Meaning that even a small amount of heat addition will cause a slight vaporization of the LNG called boil-off gas (BOG) (*Wärtsila* 2022).

A desire to utilize the BOG was one of the initial driving forces for developing combustion engines that could use gas as fuel for energy production on board the LNG tankers.

As an added benefit, running on natural gas results in a significant decrease in emissions due to its clean burning properties, low carbon content, and low content of impurities (Woodyard, 2004). Methane, which is the main component of LNG, is the most efficient hydrocarbon in terms of energy content per amount of carbon. Consequently, the emissions of CO_2 are reduced by over 20 % when running on LNG compared with other diesel fuels. Figure 1.1 presents the specific emissions from a laboratory test and field measurements on board ships in operation where LNG and MDO have been used as fuels (Æsøy et al., 2011).

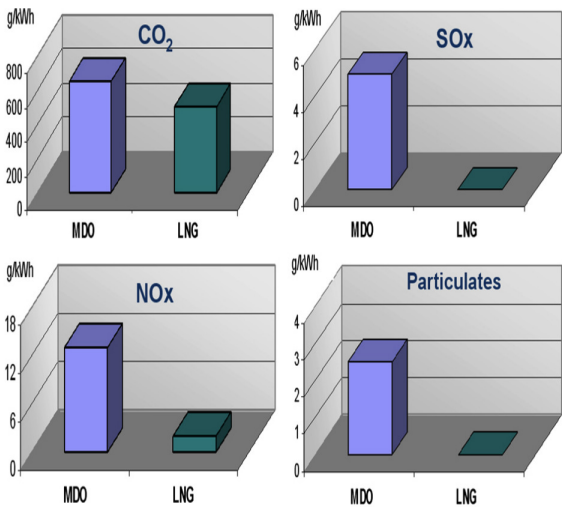

Figure 1.1: Potential emission reduction of LNG compered with MDO (Æsøy et al., 2011)

According to the study, LNG reduced emissions of CO_2 by 20-30% depending on engine load. There is also a significant decrease in NO_X due to lean combustion, as it decreases combustion temperature. The amount of SO_X and particulates are only generated from the dual fuel engines that use diesel as pilot fuels and are reduced to an absolute minimum.

1.4 Gas Engines

Different engine designs have been developed in order to ignite LNG. The engines can be split up into two qualitative different designs, namely low and high injection pressure. There are three different designs currently available: lean burn spark ignition (LBSI), low pressure dual fuel (LPDF) and high pressure dual fuel (HPDF) engines.

Lean Burn Spark Ignition Engine

The working principle of a lean burn spark-ignited (LBSI) engine is somewhat similar to the Otto cycle, and a spark ignited engine with a couple of modifications. These engines are also the most common type of diesel engines that are retrofitted to run on LNG (Æsøy et al., 2011). During the inlet stroke, gas is injected into the inlet manifold, known as port injection (PI), and mixed with air during intake resulting in a well mixed charge. However, given that there is a combustible charge in the cylinder during the compression stroke, the mixture must be very lean to reduce the risk of knocking. In addition, the cylinder head contains a small pre-combustion chamber, where a smaller amount of gas is ignited by a spark plug. The sequence is illustrated in Figure 1.2.

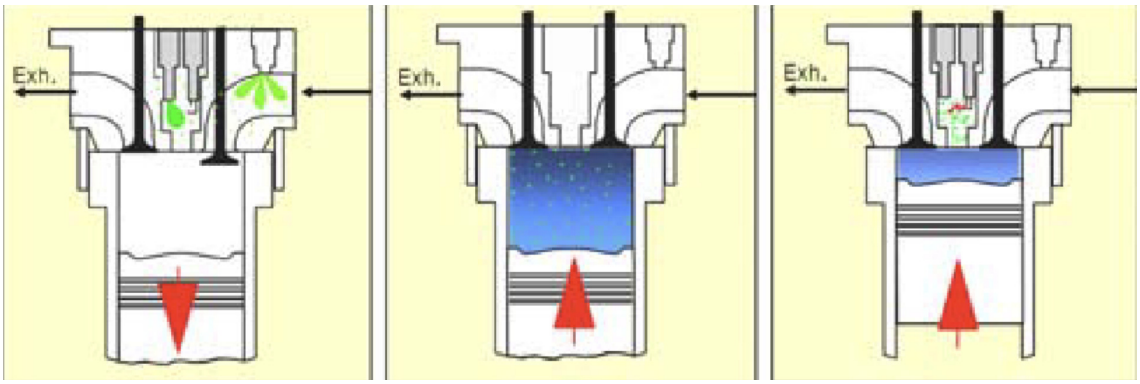

Figure 1.2: Lean burn spark engine principle

The pre-combustion chamber is necessary because the engine runs at a relatively high air excess ratio of $\lambda \approx 2$. Conventional spark plugs are not capable of operating under such lean conditions. However, in the pre-combustion chamber, a locally lower λ is obtained, providing a more steady operational condition for ignition (Stenersen and Thonstad, 2017). Operating at such lean conditions reduces the peak temperatures drastically during combustion, consequently reducing the production of thermal NO_x. However, running under too lean conditions cause its own set of problems. A lower combustion temperature may

cause quenching of the flame in the coldest parts of the cylinder, resulting in incomplete combustion of the fuel. Incomplete combustion of LNG is known as methane slip and is especially an issue at low loads.

However, LBSI engines can reach a thermal efficiency of 48-49 % at high loads, which is rather good compared to diesel engines at 40%.

Low Pressure Dual Fuel Engines

The four-stroke LPDF engine working principle combines the Otto and diesel cycle. Gas enters the cylinder in the same manner as for an LBSI engine, by being injected into the manifold just before the inlet valve and consequently mix with air during the intake and compression stroke. However, a pilot fuel injection ignites the mixture instead of a spark plug. It is also possible to use diesel as a backup fuel, which is a massive advantage of the LPDF compared with the LBSI. The working principle of the LPDF engine is illustrated in Figure 1.3

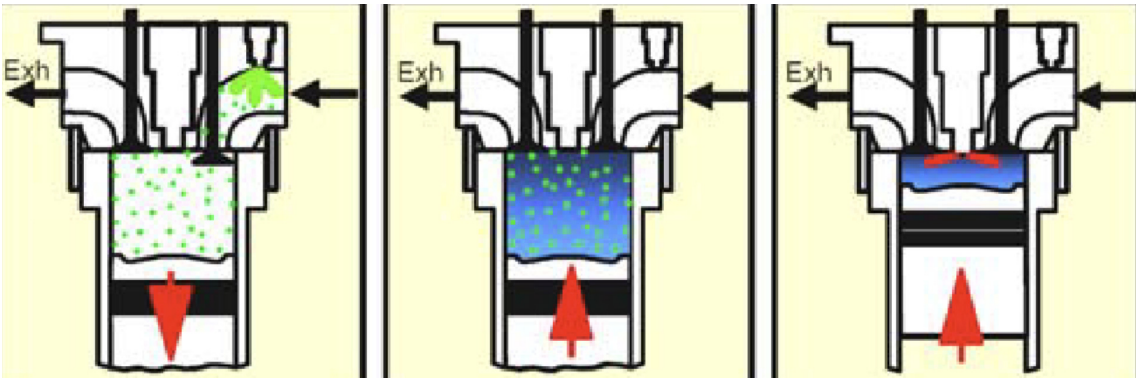

Figure 1.3: Low pressure dual fuel engine principle

Consequently, the LPDF cycle is a compromise between the Otto cycle and the diesel cycle. The compression ratio has to be large enough to ignite and assure stable combustion of the pilot injection but cannot be too large to avoid knocking. Another challenge with the LPDF is that the pilot injection needs to be as small as possible. In order to supply such a small quantity, a secondary injector, designated to only supply pilot injections, must be integrated. Typically the pilot fuel accounts for 1-3% of the energy whereas the rest comes from the gas(Stenersen and Thonstad, 2017) (Ahmad et al., 2021).

High Pressure Dual Fuel Engine

Unlike the LPDF engine, where the gas is injected prior to the inlet valve, the gas in a high pressure dual fuel HPDF engine is direct injected. Hence, the working principle of a HPDF engine can be fully described by the Diesel cycle. Still, there is a need for a pilot injection of a diesel fuel, which is injected just before top dead center (TDC) followed by a gas injection as shown in Figure 1.4.

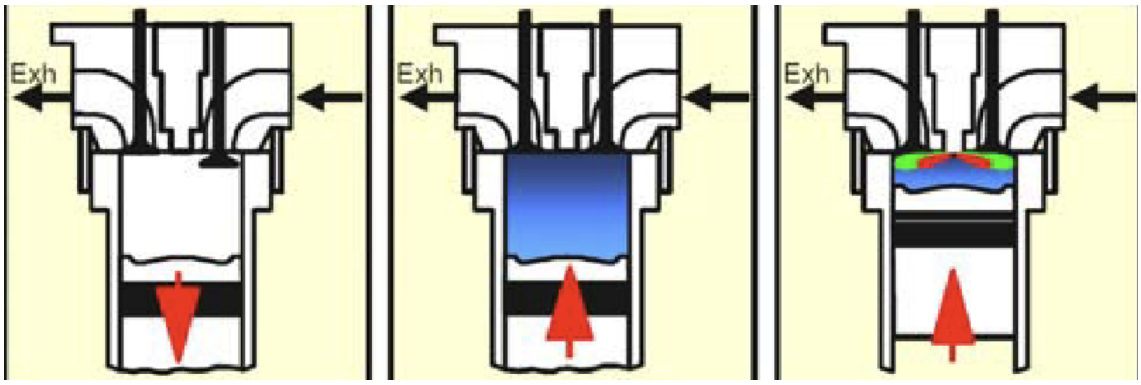

Figure 1.4: High pressure dual fuel engine principle

Since the gas is directly injected into the cylinder, the pressure at which it is injected must be higher compared to the LPDF and LBSI engine. Typically the gas is injected at between 300 and 350 bar (Stenersen and Thonstad, 2017) (Strödecke, 2015), which also poses the largest technical challenge with the HPDF engine. As mentioned in section 1.3, LNG is a cryogenic fluid. While the technology of compressing cryogenic fluids is well known, they are not designed for continuous operation, meaning that the service interval for the pumps is very high compared with other equipment on board a ship.

However, the HPDF engine has two distinct advantages over both the LPDF and LBSI engines. Firstly methane slip is reduced to a minimum due to increased combustion temperature. Secondly, there are no requirements for gas quality because there is no risk of knocking.

1.5 Gas Injections

Dependent on the engine design, the gas fuel is introduced in different manners. Common for the low-pressure engines is that fuel is introduced into the cylinder together with the charge air. However, the gas itself may be injected before or after the turbocharger. In any case, the injection pressure is relatively low, so the injection system itself is not very costly. Direct injecting gas at high pressures, however, requires significant modifications. Considering that LNG is a cryogenic fluid, specially designed heat exchangers and pumps must be implemented to reach the desired injection pressures of 300 - 350 bar.

Additionally, gas injected at high pressure has significantly different characteristics than liquid injections. When liquids are injected, they are atomized, then vaporized, and auto-ignited due to the temperature in the cylinder. However, at high pressures, compressible effects dominate the characteristics of gas jets. This introduces a set of phenomenons that are not present for liquid injections, which are considered incompressible. To mention a few, the injection pressure drops immediately when the injection starts and as fuel gets discharged. Additionally, when the pressure ratio between the injection pressure and the cylinder pressure becomes sufficiently large, the gas jet is dominated by shock structures and sonic and super-sonic velocities, which impact the mixing between the fuel and air.

1.6 Injection experiments

Measurements of cylinder pressure, torque and fuel consumption can give valuable information regarding the performance of an engine. However it provides little to none information of the actual combustion of the injected fuel. As a consequence multiple optical setups have been developed in order to study the actual flame propagation in addition to the behaviour of the injected fuel.

As sonic and supersonic flows are phenomenons that appear in numerous engineering disciplines, published studies vary in the approach and the setup, whether numerical or experimental (Golub et al., 2007) (Munday et al., 2011) (Hill and Ouellette, 1999). Concerning gas combustion engines, much emphasis is put on the characteristics of pulsed jets as it influences the subsequent flow structures and turbulent mixing downstream (Yu et al., 2013) (Dong et al., 2018) (White and Milton, 2008) (Dong et al., 2017). It has been shown that a larger injection pressure has a slight influence on the development of the penetration tip length., while the influence on cone angle is significant. Where a larger injection pressure generally corresponds to a larger cone angle (Yu et al., 2013) (Dong et al., 2018).

1.7 Scope of Work

This study presents the results from experiments conducted with a constant volume combustion chamber, where nitrogen has been injected at relatively high pressures and where schlieren imaging technique has been used to analyze the images of the jet while the instantaneous pressure over the injector has been measured during the injection. The aim is to determine the effect of the pressure drop during the injection on the macroscopic features of the gas jet.

These images have been analyzed to determine cone angle and penetration length, where the latter also indirectly provided the jet tip velocity. Together with measurements of the continuous pressure over the injector, the relation between jet behavior and injection pressure has been examined.

Chapter 2

Gas Jet Characteristics

The physical characteristics of a gas jet are highly dependent on injection pressure, velocity, and the shape of the nozzle it flows through. Considering HPDF engines where gas is directly injected, there is a relatively short time for mixing between the fuel and air. Hence the development of gas characteristics is of interest to improve combustion control. For HPDF engines, the injection pressure is relatively high compared to the ambient pressure the fuel is injected into. This leads to multiple phenomena that are not present in liquid injections, such as compressibility and shock structures.

2.1 Compressible Flow

Compressibility is a property of a fluid, stating the fractional change in volume of the fluid element per unit change of pressure (Anderson Jr., 2003). Compressibility in terms of density is defined by Equation 2.1

$$\tau = \frac{1}{\rho}\frac{d\rho}{dp} \tag{2.1}$$

Liquids have very low values of compressibility while gasses have high, for instance the compressibility of air is over four orders of magnitude larger than water (Anderson Jr., 2003). Rearranging Equation 2.1 yields

$$d\rho = \rho\tau dp \tag{2.2}$$

Consequently, from Equation 2.2, when a fluid experiences a change in pressure dp, the corresponding change in density will be dρ. However, for a given change in pressure dp, the corresponding change in density will be small for liquids, due to the small compressibility, while it will be greater for gasses with larger compressibility. As the velocity of the flow is highly dependent on the pressure gradients, liquid flows can experience relatively large changes in pressure, then also high velocities, without having any significant change in

density. Which is also the reason why liquid flows generally are assumed as incompressible. However, high velocity gaseous flows, with corresponding large pressure gradients, lead to substantial changes in density. Such flows are considered compressible or variable density flows. Generally, gas flows traveling with velocities above approximately 0.3 the speed of sound are said to be compressible (Anderson Jr., 2003).

When a flow is considered compressible or sonic, the physics of flow changes drastically compared to an incompressible or subsonic flow.

Applying Euler's equation(Equation 2.3) and continuity equation (Equation 2.4) for a steady quasi one - dimensional flow, meaning u, p, ρ, T and A is only dependent on x, through the control volume in Figure 2.1, it is possible to derive an expression of the relation between change in cross-sectional area and velocity through the control volume, called area-velocity relation (Anderson Jr., 2003). The relation is shown in Equation 2.6

$$udu + \frac{dp}{\rho} = 0 \tag{2.3}$$

$$\rho_1 u_1 A_1 = \rho_2 u_2 A_2 = constant \tag{2.4}$$

From Equation 2.4 it follows that

$$d(\rho u A) = 0 \tag{2.5}$$

$$\frac{dA}{du} = \frac{A}{u}(\frac{u^2}{a^2} - 1) = \frac{A}{u}(M^2 - 1) \tag{2.6}$$

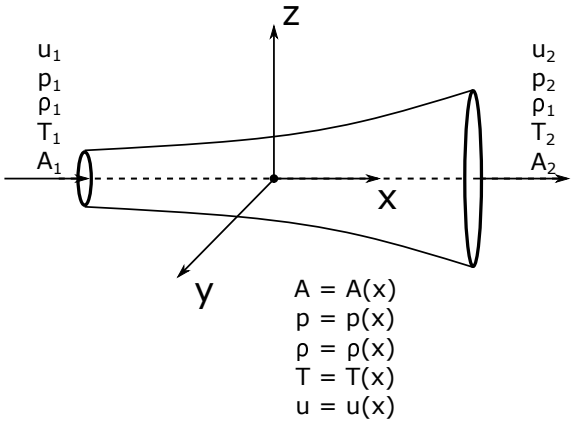

Figure 2.1: Control volume

From Equation 2.6, it is possible to get some information on how the area affects the velocity of a fluid flow. Figure 2.2a illustrates in simple terms how the area affects the velocity of a flow relative to the Mach number. When the flow is subsonic ($0 \leq M < 1$), an increase in velocity corresponds with a decrease in area and vice versa. Hence, with respect to the

area-velocity relation, a subsonic compressible flow behaves similar to an incompressible flow, where velocity increases in a converging duct and decreases in a diverging duct.

When the flow becomes supersonic ($M > 1$), an increase in velocity corresponds with an increase in area and vice versa. Hence, a supersonic flow behaves completely opposite to a subsonic flow. The velocity of a supersonic flow increases through a diverging duct while it decreases through a converging duct.

When the flow is sonic ($M = 1$), Equation 2.6 yields $\frac{dA}{A} = 0$, which implies that there is no change in area. The only physically feasible solution is the minimum area in a variable area duct. These relations are illustrated in Figure 2.2

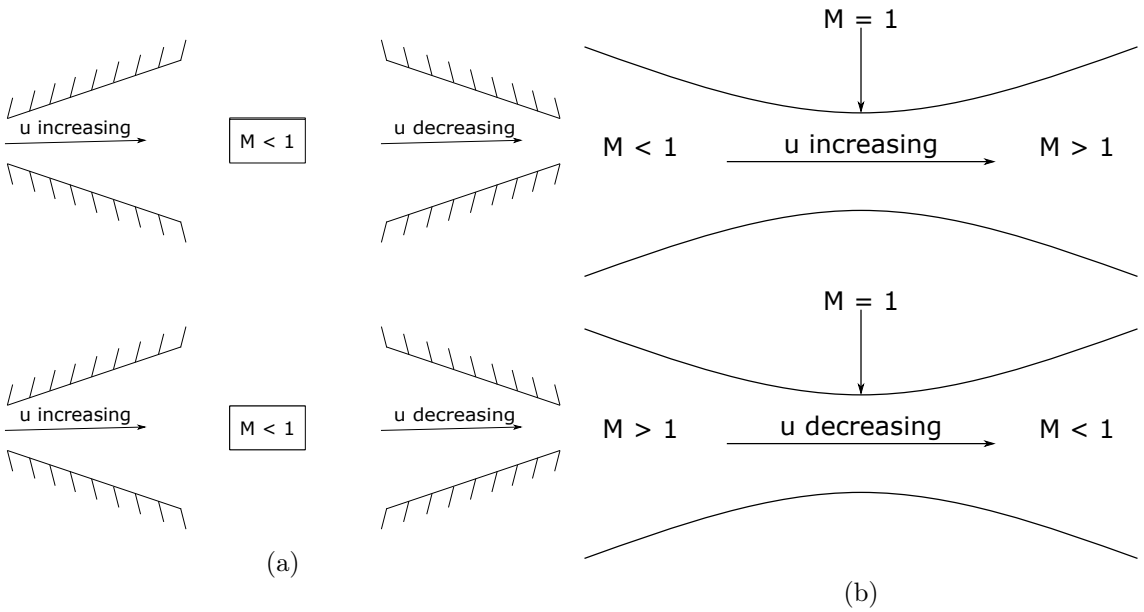

Figure 2.2: Area - velocity relations for compressible flows

When the flow at the throat of a nozzle, where the area is minimum, reaches M = 1, it becomes choked. If the upstream pressure continues to increase, no more flow will pass through the nozzle. Hence maximum mass flow through the nozzle is reached, and the flow in the exit plane becomes independent of the back pressure (Zucrow and Hoffman, 1976). This is because minor pressure disturbances travel at sonic speed, meaning that when the flow reaches sonic speed, the ambient pressure does not reach fluid in the exit plane (Zucrow and Hoffman, 1976).

2.2 Underexpanded Jets

The characteristics of gas jets discharged from convergent nozzles are highly dependent on the nozzle pressure ratio (NPR), that is, the ratio between the injection pressure and the back pressure. The ratio can also be defined by the ratio between the exit pressure from the nozzle, p_2 in Figure 2.1, and back pressure, defined as nozzle exit pressure ratio (NEPR), shown in Equation 2.7. Based on the NPR, the jet can be characterized as either subsonic,

moderately underexpanded, or highly underexpanded (Hamzehloo and Aleiferis, 2016), these are also known as the transition stages of underexpanded jets and are illustrated in Figure 2.3.

$$NPR = \frac{p_{inj}}{p_b} \tag{2.7a}$$

$$NEPR = \frac{p_e}{p_b} \tag{2.7b}$$

The term underexpanded jet is used for a gaseous fluid that is discharged through a divergent circular nozzle, into a back pressure, where the exit pressure of the jet is larger than the back pressure. The jet itself may be divided into the nearfield region, the farfield region and a transition region in the boundary between the near- and farfield.

When an underexpanded jet is issued from a nozzle into an environment with much lower pressure, it expands rapidly, which is increasing the cross-sectional area of the jet. This rapid expansion creates a normal shock wave relative to the direction of the flow, is prominent near the nozzle. Research have shown that an increase in NPR, for an already highly underexpanded jet, increase the width of these shock waves, which in turn increase the cone angle of the jet. A large cone angle is preferable considering improved mixing of the jet and the surrounding air (Dong et al., 2017).

When the pressure ratio between the exit pressure and back pressure reaches what is called critical expansion ratio, given in Equation 2.8, the velocity of the flow reaches the local speed of sound at the location where the cross-sectional area of the jet is at its minimum.

2.2.1 Characteristics of Underexpanded Jets

As previously mentioned the transition stages of underexpanded jets are known as subsonic, moderately underexpanded and highly underexpanded. Figure 2.3 illustrates the different characteristics of these jets.

$$\frac{p_e}{pinj} = \frac{p^*}{p_{inj}} = (\frac{2}{\gamma + 1})^{\frac{\gamma}{\gamma - 1}} \tag{2.8}$$

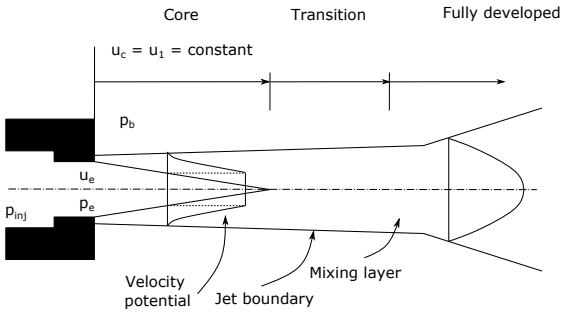

(a) Subsonic stage

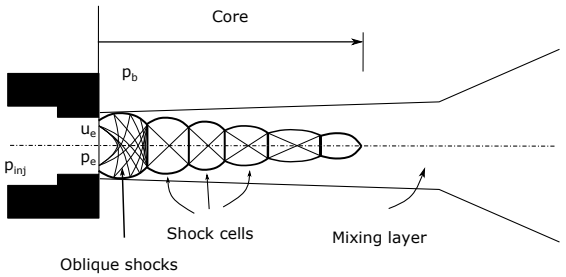

(b) Moderately underexpanded jet

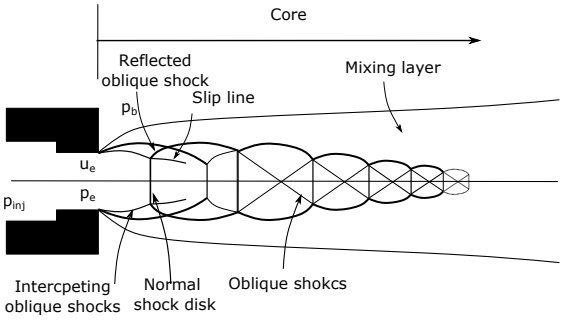

(c) Highly underexpanded jet

Figure 2.3: Schematic of underexpanded jets based on (Donaldson and Snedeker, 1971) (a) Subsonic jets: $1 < p_{inj}/p_b < 1.9$, (b) Moderately underexpanded jets: $1.9 < p_{inj}/p_b < 3.8$ (c) Highly underexpanded jets: $3.8 < p_{inj}/p_b$

A subsonic jet is characterized by a potential core surrounded by a mixing region where the jet and the surroundings are interacting and mixed. At multiple nozzle diameters downstream, the mixing layer has advanced inward to the center line of the jet, and consequently the core ceases to exist. Beyond this point, the mixing layer continues to spread as the jet develops (Donaldson and Snedeker, 1971) (Hamzehloo and Aleiferis, 2016) (Franquet et al., 2015), illustrated in Figure 2.3a.

As the pressure at the exit of the nozzle, p_e, increases, the characteristics of the jet change. When the critical pressure in the jet is reached and NEPR $\approx$ 1.1 - 2, what is known as shock cells forms near the nozzle exit consisting of intersecting oblique shocks. These

occur because the jet has to expand to equalize the ambient pressure. When that has occurred, compression waves are reflected toward the center of the jet, where they coalesce and form oblique shocks, known as intercepting shocks. The shock structure forms the core of the jet, and the boundary is dependent on the requirement of equilibrium between the pressure in the shock cells and the ambient. This is why the shock cells will decrease in size downstream in the jet because the pressure ratio of the cells and ambient decreases. As for subsonic jets, the inward diffusion of the mixing layer will cause the core to dissipate, and the further development of the jet is expected to behave similarly to a subsonic jet from this point on (Donaldson and Snedeker, 1971) (Hamzehloo and Aleiferis, 2016) (Franquet et al., 2015). .

When the NEPR is increased even further to NEPR > 2, the structure of the initial shock cell changes. When the pressure ratio increases, the coalescing of the compression waves no longer occurs at the center line. Moving along the center axis of the initial shock cell in Figure 2.3c, the minimum pressure, located at where the expansion is maximum, becomes too low for the compression waves to coalesce into an oblique shock. Instead, the required compression takes place through a visible normal shock disk relative to the jet, known as a Mach disk. Following the Mach disk, a slip line separates the flow through the disk, which has become subsonic, from the reflected shock, which still is supersonic. Dependent on the degree of underexpansion, multiple Mach disks may appear because the subsonic flow behind the normal shock quickly is accelerated to supersonic, and the same sequence occurs again. Either way, an increase in NEPR will result in a more visible and wide Mach disk (Donaldson and Snedeker, 1971) (Hamzehloo and Aleiferis, 2016) (Franquet et al., 2015).

2.3 Macroscopic Features of Jets

Macroscopic properties of gas jets typically include spray angle, known as cone angle, jet penetration length and speed. The cone angle is often defined as the angle between two lines that encloses the spray in the radial direction. While the penetration length is generally defined as the distance from the nozzle tip to the front edge of the gas jet (Yu et al., 2013) (Hill and Ouellette, 1999) (Dong et al., 2018). Hence, the jet speed is defined as the speed at which the jet tip propagates. Both cone angle and penetration length are illustrated in Figure 2.4.

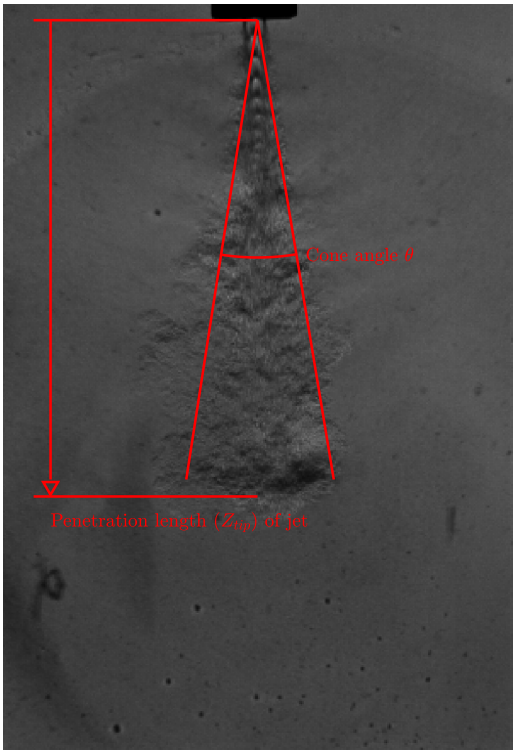

Figure 2.4: Illustration of cone angle and penetration length

A large cone angle and penetration length will increase the jet volume and therefore increase the air utilization, resulting in a more effective mixing. While the penetration length might be limited by wall impingement (Haji et al., 2016). Due to the impact, these features have on the jet's mixing properties, accurately determining them can provide helpful information for injector designers and numerical models. Additionally, analyzing how they develop during a transient state can also be valuable.

Chapter 3

Optical Measurement Techniques

As previously mentioned, in section 1.6, measurements such as cylinder pressure, torque and fuel consumption can only give a limited understanding of the physical process that occurs prior to and during fuel combustion in an engine. Hence, a wide variety of optical measurement techniques have been developed to visualize the development of injection. Where some of the most commonly used are shadowgraphs, interferograms, planar laser-induced fluorescence (PLIF) and schilieren.

3.1 Schlieren

Schlieren imaging is an optical manipulation technique that makes it possible to see transient gas currents, temperature gradients, pressure differences and different compositions of gasses. The human eye can only register the amplitude, colour and in some cases, polarization of a light beam. However, the schlieren method allows for perceiving phase changes in a light beam. The schlieren method relates thermodynamic properties of transparent fluids with their refractive index. It dates back to the 17 th century and is still a widely used method to study inhomogeneous fluid flows (Settles, 2001).

It usually consists of a light steering device, such as a concave mirror or a combination of lenses, a light source, a sharp edge, such as a razor blade, and a camera. Though the setup varies slightly, depending on whether a mirror or a combination of lenses is used, the principle remains the same.

For a setup with lenses, the light from the source spreads out but is made parallel through the first lens, then it passes through the test area where the light is refracted before it passes through a second lens. The second lens collects the light into a point where a sharp edge is placed, cutting off approximately half of the light. Such a setup is illustrated in Figure 3.1.

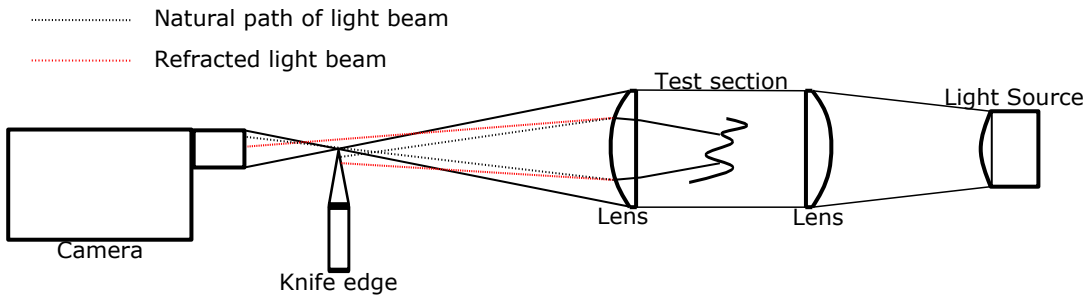

Figure 3.1: Schematic of optical schlieren with lenses

For a setup with mirror(s), the light spreads out and is reflected back toward the camera, through the test area which is close to the mirror. As for the lens setup, the shape of the mirror collects the light to a point, where a sharp edge cuts off some of the light. A schematic of optical schlieren with mirror is shown in Figure 3.2.

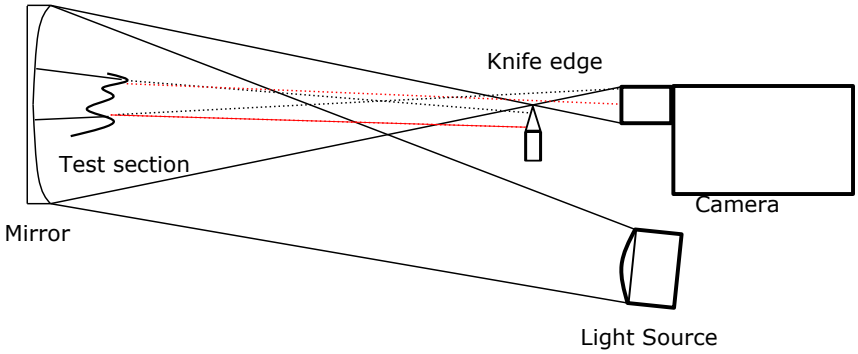

Figure 3.2: Schematic of optical schlieren with mirror

If a medium, such as a gas jet or burning candle, is placed in the test section, the light will refract slightly due to the change in refractive index. Some of the light that normally passes over the knife edge will hit the edge, while some that would usually pass under the is refracted over and into the lens. It is this effect that makes it possible to detect the phase changes in the test section.

The Gladstone-Dale equation, which is seen in Equation 3.1, express a linear relation between the density of a fluid and its refraction index.

$$n - 1 = k\rho \tag{3.1}$$

Where n is the refractive index, k is the Gladstone-Dale constant and ρ the fluid density. Additionally, if the fluid is a gas and do not deviate to much from atmospheric conditions, it is possible to assume that the properties of the gas can be described by the the ideal gas equation of state Equation 3.2 (Moran et al., 2015).

$$P = \rho \bar{R} T \tag{3.2}$$

Where $\bar{R}$ is the universal gas constant. Combining Equation 3.1 and Equation 3.2 the

effect pressure and temperature have on the density and how it relates to the refractive index is obvious. However, for gaseous fluids due to their relatively small density, n is weakly dependent on density. For air, a change of density in the order of 2 will only have a slight effect on the refractive index, about 3 % (Settles, 2001).

Due to the small change of refractive index, the schlieren method require a high quality set up, in the form of high sensitive optics.

Chapter 4

Experimental Set Up

In order to get a fundamental understanding of how a spray, for liquid fuels, or the jet, for gaseous fuels behave once they are injected, a series of optical experimental setups have been developed. The different arrangements aim to analyze or replicate different phenomena that occur in a combustion engine.

A constant volume combustion chamber (CVCC) was used for the experiments conducted in this thesis, and is shown in Figure 4.1. This setup could perform injections of either liquid or gaseous fuels.

The CVCC was also equipped with a pre-combustion system, where a spark can ignite a combustible gas mixture in order to create engine-like conditions, which again allows for auto-ignition of injected fuels. However, during this thesis's preliminary study, the pre-combustion system was discovered to have several major safety violations. Hence, it was not used for the experiments conducted, which means that the tests were nonreactive.

Still, the CVCC allows for high repeatability with respect to the conditions that liquid or gas are injected into, and nonreactive experiments can be used to determine macroscopic features and shock structures of underexpanded jets.

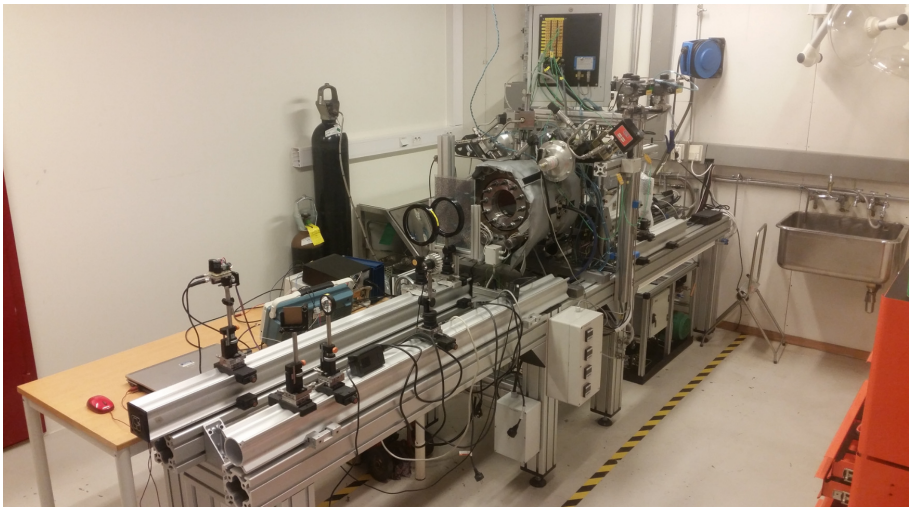

Figure 4.1: Picture of the experimental setup. (Set up for BOS imaging in this picture)

4.1 Description of Test Bed

4.1.1 Chamber

In simple terms, the combustion chamber consists of a cylinder lying horizontally that has a volume of 6.8 dm^3. The chamber is sealed by two sapphire windows allowing for optical accessibility. Additionally, eighth slots are evenly spaced around what can be defined as the cylinder wall, which makes it possible to install instruments, such as injectors, spark plugs, fan, exhaust- and inlet valves and sensors. A CAD model of the chamber is shown in Figure 4.2

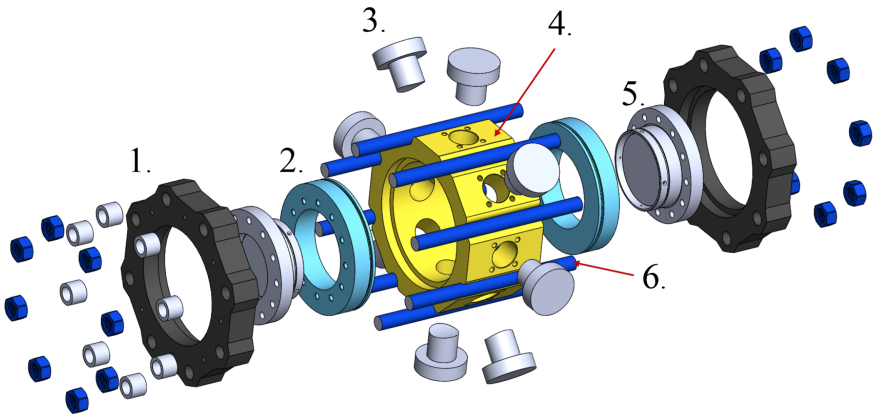

Figure 4.2: CAD model of Chamber (1.Bracket; 2.Wall; 3.Plug; 4.Main body; 5.Window; 6.Anchor bolt)

During the preliminary study of this thesis, the chamber was pressure tested to check for leaks and to verify the integrity of the chamber. The chamber was filled with water and pressurized to 265 bar. An additional leakage test was conducted using nitrogen, where

the chamber was pressurized to 50 bar.

4.1.2 Injector

The gas injector was designed and developed at NTNU. It is a high pressure injector capable of injecting at pressures up to 400 bar, thus also capable of injecting at pressures that are used for HPDF engines (Krivopolianskii, 2019). However, the injector suffered from a severe leak from pressures above 150 bar, which restricted the pressure used for the experiments.

The exterior of the injector is shown in Figure 4.3 with its main components. It is worth mentioning that the needle lift sensor was not in use during the conducted experiments. The internal design of the injector is shown in Figure 4.4

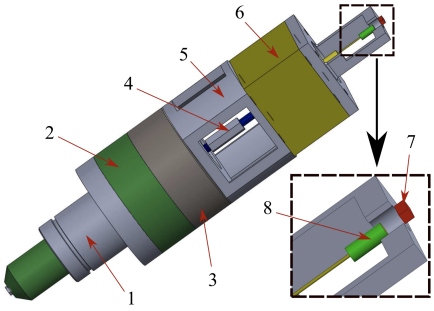

Figure 4.3: External design of high pressure gas injector, 1.Adapter, 2.Nozzle, 3. Holder, 4.Needle connector, 5.Hydraulic servo-valve mount, 6.Hydraulic cylinder and hydraulic servo-valve, 7. Needle-lift sensor, 8. Magnet

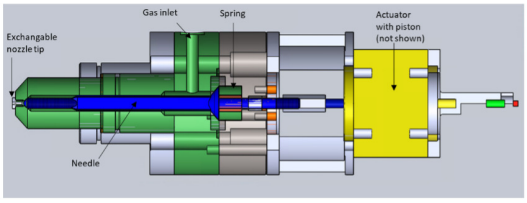

Figure 4.4: Internal design of injector

The adapter is the injector part that seals off between the chamber and injector. The hydraulic servo valve, a fast acting hydraulic servo valve delivered by MOOG, is the actuator of the injector. When the injection signal is given, hydraulic fluid, at about 200 bar, is directed to the lower side of the piston, creating a force that lifts the needle. When the injection signal stops, the fluid is redirected to the other piston at the top, which pushes the needle down. Additionally, the needle is kept in a closed position by a compressed spring in the form of ten Belleville washers stacked on top of each other. In addition, the nozzle tip is easy to replace, making it possible to use different nozzle geometries.

4.1.3 Gas Supply System

The gas supply system was developed in order to assure a controlled sequential filling of the chamber with combustible gasses or inert gasses if pre-combustion is not desired. The schematic illustrated in Figure 4.5, shows how the gas supply system is assembled. As

shown, the system is divided between two separate rooms. The green part illustrates the laboratory where the chamber itself and control room are, while the purple illustrates the bottle room, where the gas bottles are stored and the mixing of supply gasses is done.

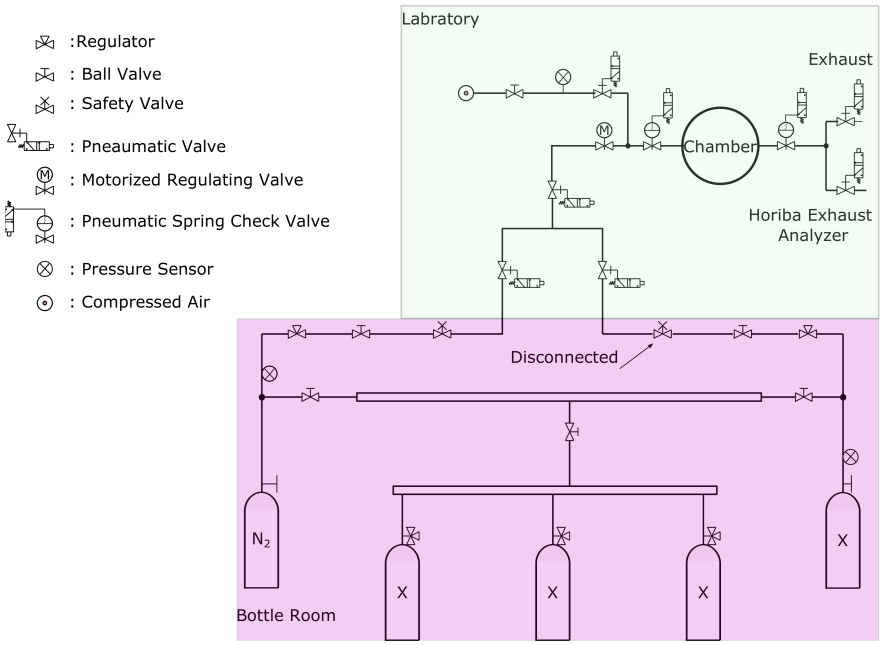

Figure 4.5: Gas supply system

Even though no experiments with combustion were conducted in this study, it was necessary to understand the gas supply system completely. This was because during this thesis's preliminary study multiple factors regarding safety and operability were discovered to be unsatisfactory. For example, as indicated in the figure, one of the safety valves was disconnected and bypassed but had not been documented anywhere.

There are possible to connect a total of five gas bottles to the system. The three bottles in the center of the purple section are used as feeding bottles to the bottles furthest out, called mixing bottles. These feeding bottles are typically filled with an oxidizer, such as oxygen(O_2) and a combustible gas, such as carbon monoxide (CO), in addition to nitrogen (N_2). Then, based on partial pressures, one mixing bottle can be filled with a combination of nitrogen and oxygen, simulating air, while the other contains a combustible mixture. This is needed in order to create similar conditions in the chamber that occurs in an engine by burning these gas mixtures. In addition, pre-combustion is necessary in order for diesel fuel to self-ignite.

The bottles marked with X were disconnected during the execution of the experiments and only nitrogen was used.

The gas was transported into the chamber by a network of pipes and valves. The opening and closing of valves from the safety valve and to the exhaust valves are done automatically from the control sequence implemented in the control software.

4.1.4 High Pressure Gas Injection System

The gasses that are injected into the chamber stored at standard gas cylinders, with a maximum pressure of approximately 200 bar. However, as mentioned in subsection 4.1.2 the injector is capable of operating with injection pressures up to 400 bar, therefore a compression stage in the gas supply system has been developed.

A schematic of the developed system is shown in Figure 4.6.

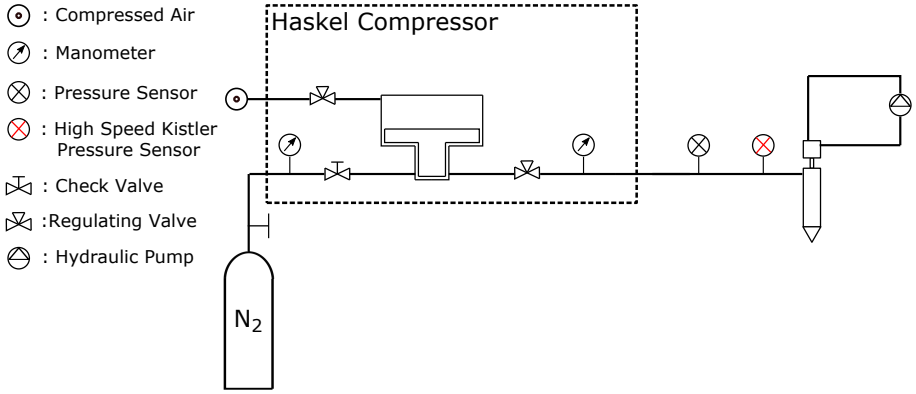

Figure 4.6: High pressure injection system

As can be seen, there are two separate circuits. One containing the injection gas and the other with compressed air. The compressed air is used to push a piston, with a relatively large surface area, that are connected to a smaller piston. The smaller piston is part of the injection gas circuit, utilizing Pascals law, Equation 4.1, it is possible to increase the pressure in the gas injection circuit.

$$p_1 = \frac{F_1}{A_1} \leq p_2 = \frac{F_2}{A_2} \tag{4.1a}$$

$$A_1 > A_2 \tag{4.1b}$$

The regulation of the injection pressure had to be done manually and because of the leak had to be regulated ahead every injection. As a consequence, the time between injections increased considerably.

High Speed Pressure Sensor

The injection pressure was measured using a piezoresistive pressure sensor, delivered by Kistler. The pressure was processed through an amplifier with a sampling frequency of 40 kHz, meaning that there was taken a measurement of the pressure every 0.025 ms. The total sampling period was 25 ms, which sufficient for the experiments that was conducted in this study.

The Kistler sensor was mounted between the gas feeding pipe and the gas inlet on the injector. The sensor was necessary in order to get a more complete sampling area during the actual injection. The sensor that was mounted prior had a sampling frequency of 4 kHz, making the Kistler sensor ten times faster.

4.1.5 Control System

The control and data acquisition of the experiments are based on the CompactRIO system delivered by National Instruments. The user interface is accessible from a GUI panel developed in LabVIEW. The GUI panel allows for monitoring pressures and temperatures. In addition, it was used to initiate the injection, determine injection- length and pressure for liquid fuels, pressurize the chamber with the desired gasses to get optimal injection conditions, start the mixing fan, purge the chamber with compressed air and switch on the heating elements. This study did not use heating elements, the mixing fan or liquid fuels.

The measured data from each experiment were exported to excel.

4.2 Optical SetUp

In Figure 4.7 the setup used, for imaging the schlieren effects of the jet, is shown. As can be seen, it consisted of a camera, knife edge, two plano concave lenses, the CVCC as test section and a very powerful LED light.

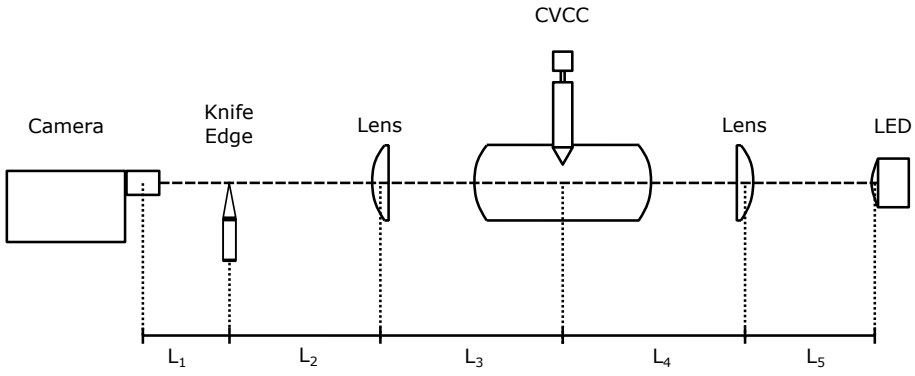

Figure 4.7: Sketch of optical setup

The distance between each element in the set up is shown in Table 4.1

Table 4.1: Distances between components of the optical set up

Segment	Distance [mm]
L_1	90
L_2	845
L_3	320
L_4	320
L_5	1220

In order for the LED to emit enough and constant light during the injection, it had to be synchronized with the exposure time of the camera, illustrated in Figure 4.8. By doing so the LED was set up to flash periodically, instead of continuously, which allowed for setting a higher voltage on the LED resulting in a brighter light. In turn this allowed for reducing the exposure time of the camera providing a less blurry image of the jet.

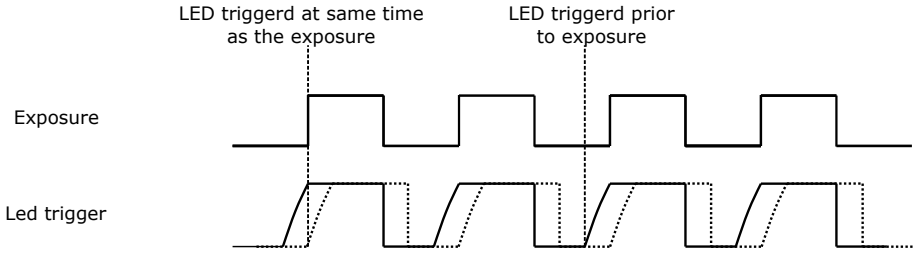

Figure 4.8: Synchronization of LED and camera exposure

An important aspect regarding triggering of the LED is that it has to be initiated slightly ahead of the exposure signal for the camera. This assures that the LED is at its brightest over the whole period the lens is exposed and that each frame has the same amount of light throughout.

The equipment used for the optical schlieren set up are summarized in Table 4.2

Table 4.2: Optical equipment and parameters used for schlieren arrangement

Element	Description
Camera	Photron SA-X2
Camera lens	Nikon 105mm, aperture ratio: 1:2.8
Knife edge	Razor blade
Lenses	Two plano convex lenses, D = 145 mm
LED	Green photo-electric pulsating diode
Frame rate	40000 fps
Exposure time	5 - 10 μs

4.3 Test Conditions

There are multiple approaches that can be used for studies of underexpanded jets, both regarding optical image capturing methods, but also for the injection conditions. Most of the experimental research available are studies for non reacting sprays, where spray development are of interest (Yu et al., 2013), (Dong et al., 2018) (Dong et al., 2017) (CRIST et al., 2012) (GRAUR et al., 2004). However, given that underexpanded jets are a phenomenon that occurs in several physical disciplines, as discussed in section 2.2, the test conditions that are used are dependent on what discipline that are of interest.

This study aims to observe and quantify the influence of dynamic injection pressure on gas fuel injection jet. Hence, it would be desirable to have test conditions that can simulate the conditions that would occur in an gas engine prior to injection.

4.3.1 Chamber Conditions

Multiple different aspects can be simulated for these types of experiments. For instance, it is possible to use NPR as a measure solely. Then it is possible to reach NPR above 100 if the back pressure is kept close to atmospheric conditions and thus obtain very highly underexpanded jets. However, this does not simulate the charge pressure, density or temperature in a CI engine. In order to simulate the charge conditions that occur in a gas engine, it was decided to use density. The charge density in an engine will vary dependent on the load and engine type, whether it is four- or two-stroke, and typically ranges between 16 to above 60 kg/m^3 between idling and full load.

Additionally, it was decided to use nitrogen as the chamber gas. This was for multiple reasons, but mainly for economic and safety reasons.

Based on these two decisions, in addition to the restriction, the leak from the injector put on injection pressure, the rig was pressurized to 25 bar for every experiment. This resulted in a density of approximately 28 kg/m^3 for an ambient temperature of 20 °C using Equation 3.2.

4.3.2 Injection Conditions

Initially, the experiments were supposed to be conducted with injection pressures similar to those found in HPDF engines, at approximately 300 bar. However, during the preliminary study of the thesis, the injector was discovered to suffer from a significant leak at pressures above 150 bar. This became a limiting factor of the test conditions that were feasible to use.

Even though the injector was designed for pressures up to 400 bar, the injection pressures used in this study were limited to 80, 130 and 150 bar, because of the leak. Which corresponded to a NPR of 3.2, 5.2 and 6, respectively. As for the chamber gas species, nitrogen was used as the jet gas species.

4.3.3 Summary of Test Conditions

Table 4.3 Summarizes the conditions that were used for the injection.

Table 4.3: Experimental parameters

Parameter	Value
Ambient temperature [K]	293
Ambient Pressure [bar]	25
Injection pressure [bar]	80, 130, 150
Nozzle pressure ratio (NPR) [-]	3.2, 5.2, 6
Injection pulse length [ms]	1
Nozzle orifice diameter [mm]	2.04
Jet gas species [-]	Nitrogen (N_2)
Chamber gas species [-]	Nitrogen (N_2)

Chapter 5

Test and Analysis Procedure

Two qualitatively different data sets were collected from the experiments and processed for further analysis. The first was a set of pictures captured by a high-speed camera, referred to as optical measurements. The second was measurements of injection pressure, in addition to the pressure inside the chamber, and are referred to as intensive measurements.

For both the optical and intensive measurements the average values of the experiments for each set was used for further analysis. However, the results from each experiment is included in Appendix B.

5.1 Post-Processing of Optical Measurements

Although optical schlieren requires high sensitive optics and are sensitive to the setup, one of the benefits of using optical schlieren is that the post-processing is less time consuming compared with other methods. For instance, it was possible to visually inspect the images to determine the start of injection, development of Mach disks and the jet propagation. However, in order to determine cone angle and penetration length, a Matlab script was developed.

5.1.1 Post-Processing of Images

In short, the desired images are imported as grayscale images and stored as a matrix. The matrix has the same size as the resolution of the original images, with values between zero and one, where zero is entirely black, and one is completely white. In order to make the jet more prominent, it was necessary to perform a background subtraction. This was accomplished by first converting the images, meaning to make the dark parts of the picture brighter and the bright parts darker. This was necessary due to the fact that the images themselves were very dark, and by doing so, the background subtraction became much more effective. As it turned out, the best results were obtained when the reference picture for the subtraction was the preceding image, consequently this was implemented

for each frame. Even so, when the jet was fully developed and the nearfield region had become steady, this region was less defined. However, with the aim of determining the cone angle and penetration length, the unclear nearfield region did not cause any significant problems. This was because the self-similar region became better defined, and the amount of disturbance was reduced.

An additional script was developed to crop the images to get the nozzle in the center of the picture/matrix. In addition, this script also calculated the picture sequence that was to be analyzed.

After the background subtraction, the picture was binarized by applying a threshold, which was obtained by using a built-in Matlab function based on Otsu's method. This is an independent and automatic method of suggesting a threshold for grayscale images to distinguish between foreground and background (Otsu, 1979) (Sezgin and Sankur, 2014). Further, the picture was binarized by using the suggested threshold, where every cell in the matrix with a value above the threshold was set to one (white), and a value below was set to zero (black). During the injection, a lot of pressure waves and density gradients appeared in the chamber. Even though the threshold value removed most of the noise, it was necessary to develop a filter.

In order to remove the noise generated by the shock waves, the first step was to use the previous image in the series as the reference picture for the background subtraction instead of an undisturbed image. Even though this made the steady part of the jet less defined, it was necessary in order to remove noise surrounding the jet. Next, a connectivity matrix was made to count the number of connected cells. However, for this to work, the image had to be converted back, meaning that the jet became white while the background was turned black. The connectivity matrix counted the number of connected white cells and stored their size and location. Based on these values, the filter set every pixel to be black, as long as they were connected to less than a predetermined value. This value was determined by checking multiple conditions, such as where in the image the pixels were, how many pixels were present, and their relative size, to name a few. By doing this, the noise was eliminated, and the chance of arbitrary pixels becoming a part of the final image was reduced.

The sequence is shown in Figure 5.1.

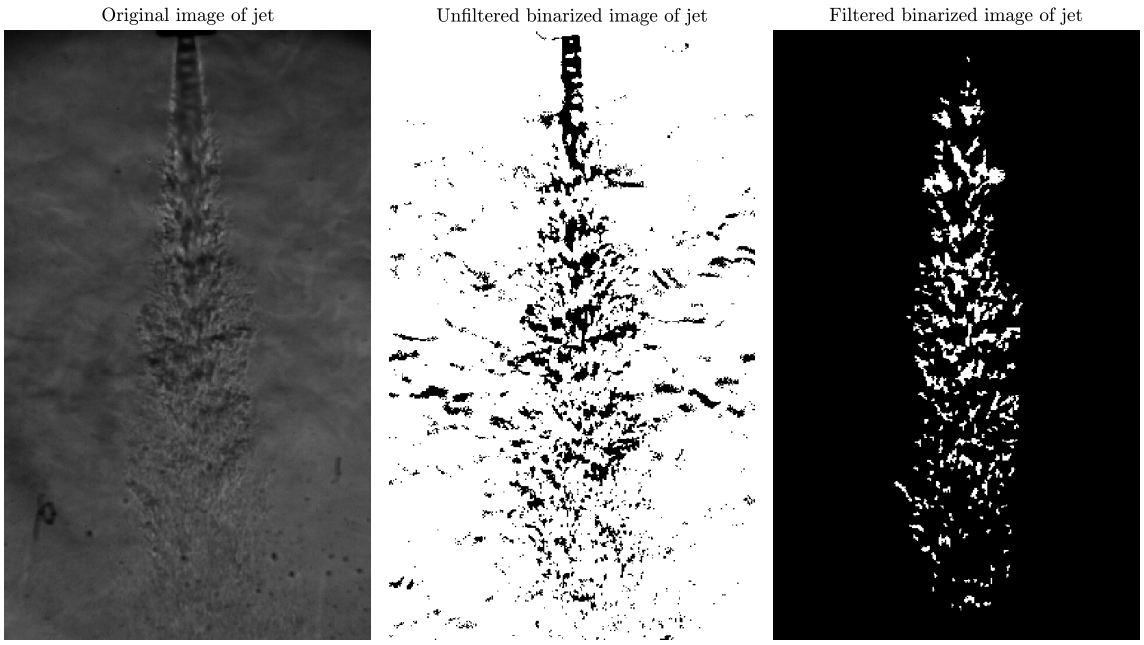

Figure 5.1: Illustration of post processing of images. The original image is not treated in any way other that being cropped in order to get the nozzle in the center of the image. The image is binarized by using Otsu's method. In order for the filter to work the binarized image had to be inverted. The filter removed clusters of pixels less than a predetermined value.

As previously mentioned, the nearfield region becomes more undefined, while the farfield region of the jet gets a well-defined edge. This is desirable for the analysis of the macroscopic features of the jet.

5.1.2 Determination of Penetration Length

The penetration length was defined as the length from the nozzle tip to the edge of the jet front and is illustrated in Figure 5.2. However, the images were imported as 512x512 pixel images so that the coordinate axes had pixels as their unit. Consequently, it became necessary to determine the length of each pixel to calculate the penetration length. This was done by using the width of the nozzle, which was known from the laboratory, and dividing it by the number of pixels it used. With this relation established, it was possible to determine the penetration length by multiplying the pixel furthest away from the nozzle with the pixel length.

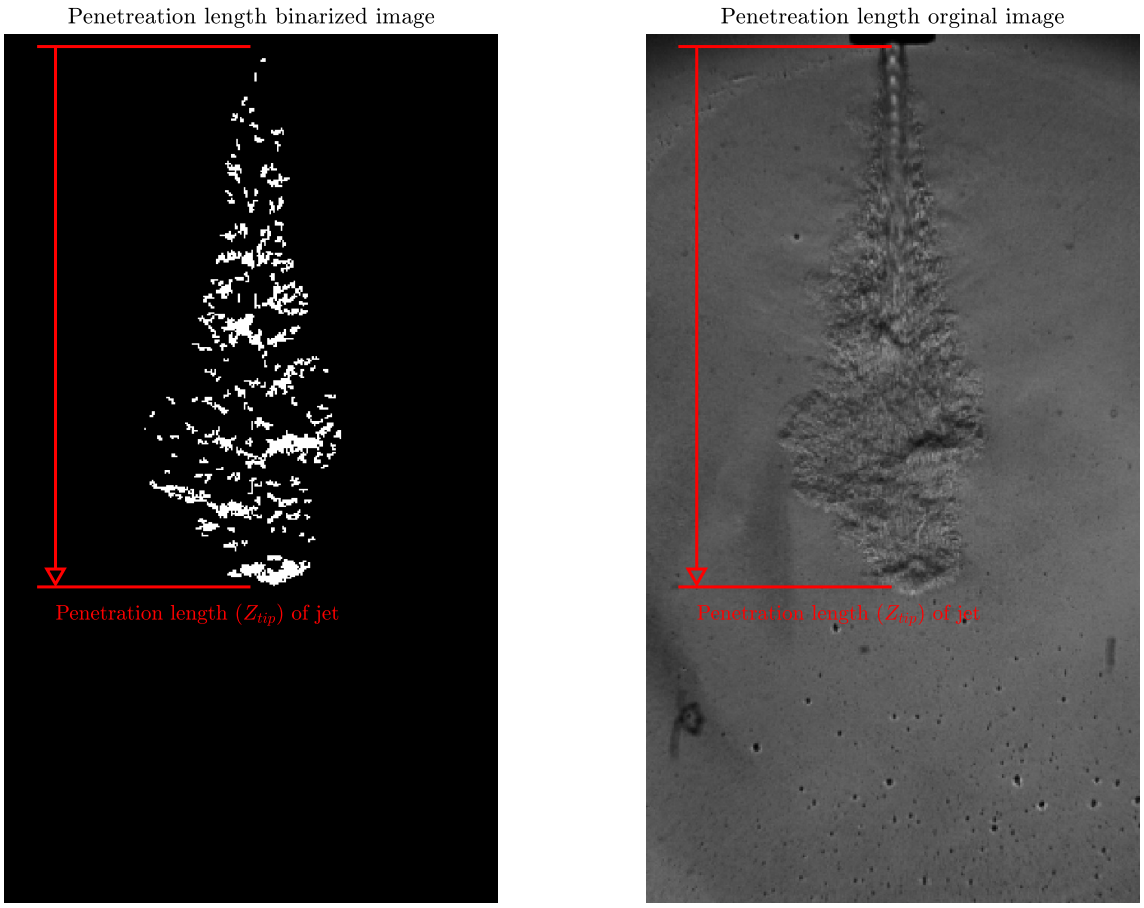

Figure 5.2: Illustration of how cone angle is determined

The pixel furthest away from the nozzle in each frame was determined by using the centroids. The centroid of interest was the one with the largest y-value. In order to eliminate the chance of a stray pixel being used as the length pixel, several conditions had to be met. This was done as an extra measure should the filter have failed to remove pixels that were not part of the jet.

5.1.3 Calculation of Jet Tip Velocity

The jet tip velocity follows naturally from the penetration length and is calculated using Equation 5.1.

$$u_{tip} = \frac{Z_{tip}(t_2) - Z_{tip}(t_1)}{t_2 - t_1} = \frac{\Delta Z_{tip}}{\Delta t} \tag{5.1}$$

However, due to the relatively poor resolution of the camera in combination with the high frame rate, the velocity calculation was very sensitive. A small difference in ΔZ_{tip} from one time step and the next had a significant impact on the velocity. When Δt was set to 0.025 ms, which was the short possible time interval, a relative difference of 0.5 mm of the jet penetration length changed the velocity with 20 m/s. Hence, the sensitivity to small

changes and the rapid changes of the jet from frame to frame causes the large variance of the velocity, seen in Figure B.13.

Due to this sensitivity, the velocity was calculated using a larger step size of 0.05 ms to reduce the effect of the sensitivity. Additionally, a moving average was applied to further decrease the large variance.

5.1.4 Determination of Cone Angle

The binarization was necessary in order to determine the cone angle. When the image was binarized, it became possible to locate the coordinates of the centroid of each pixel cluster. The cone angle was defined as the angle between two lines from the center of the nozzle to the centroids, that was furthest away from the center ion radial direction. As it turned out, these centroids were obtained by implementing a number of conditions, such as that they had to be further out than the average for the respective half of the nozzle. Mostly because, should the filter have failed to eliminate arbitrary pixels they could impact the calculated angle. Additionally, the script started looking for the centroids at two thirds of the current penetration length.

This process is illustrated in Figure 5.3 and Figure 5.4.

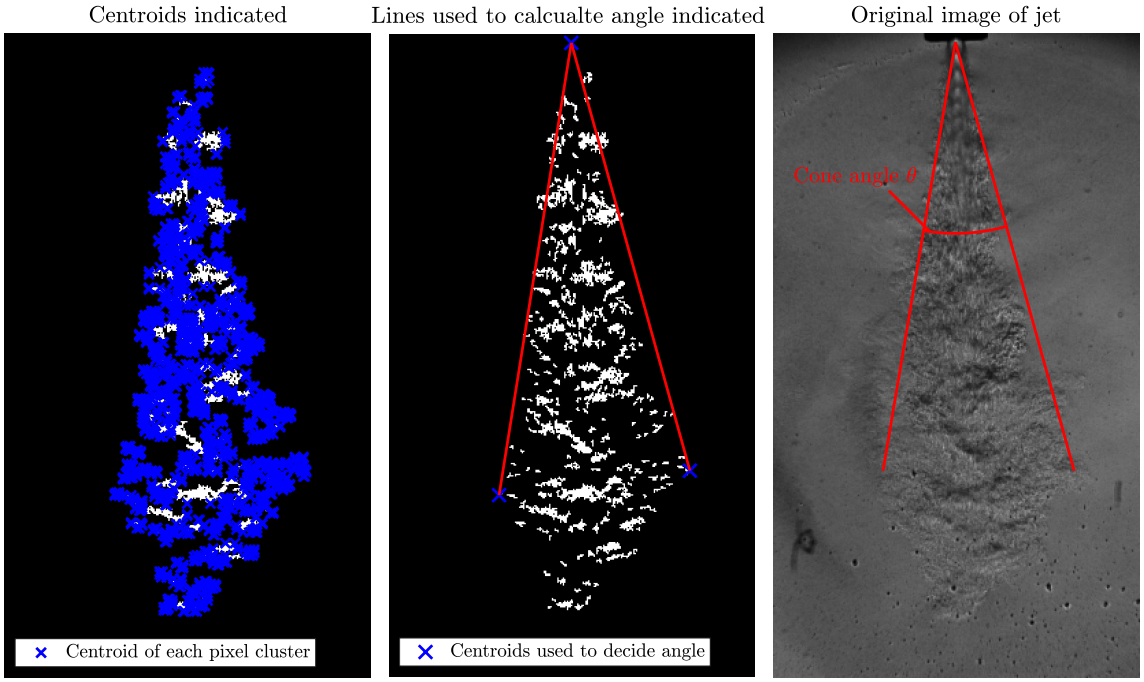

Figure 5.3: Illustration of how cone angle is determined

In Figure 5.3, the first picture shows every centroid for each of the pixel cluster, the second picture shows the three centroids that were used to calculate the cone angle, together with the lines drawn between them. The last picture shows how the lines corresponds with the actual jet.

The angle itself was calculated by simple vector trigonometry shown in Equation 5.2.

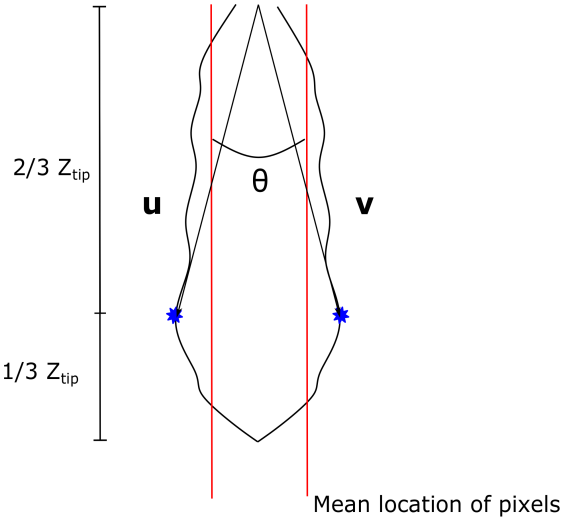

Figure 5.4: Vectors used for calculating cone angle

$$cos(\theta) = \frac{\mathbf{u} \cdot \mathbf{v}}{||\mathbf{u}||||\mathbf{v}||} \tag{5.2a}$$

$$sin(\theta) = \frac{||\mathbf{u} \times \mathbf{v}||}{||\mathbf{u}||||\mathbf{v}||} \tag{5.2b}$$

$$tan(\theta) = \frac{sin(\theta)}{cos(\theta)} = \frac{||\mathbf{u} \times \mathbf{v}||}{\mathbf{u} \cdot \mathbf{v}} \tag{5.2c}$$

The developed script seems to slightly underestimate the angle of the jet. This was a consequence of eliminating the chance of arbitrary noise and shock waves to be interpreted as the jet.

5.2 Post Processing of Intensive Properties

The main focus of this experiment was on the pressure measurements that was made by the dynamic Kistler sensor. However, properties such as temperature inside the rig as well as the pressure, were closely monitored in order to keep the conditions as equal as possible for every experiment.

5.2.1 Post Processing of Pressure Measurement

As mentioned in subsection 4.1.5 all of the measurements from each experiment were exported to excel. In order to interpret the data, a Matlab script was developed. There were two pressures of interest: the dynamic pressure over the injector and the pressure inside the chamber. After the desired values had been imported, a moving average (MA) was taken of them in order to smooth out the curves illustrated in Figure 5.5 and Figure 5.6. For the injection pressure, the average was calculated over 50 measurement points, while the chamber pressure was calculated over 170 points.

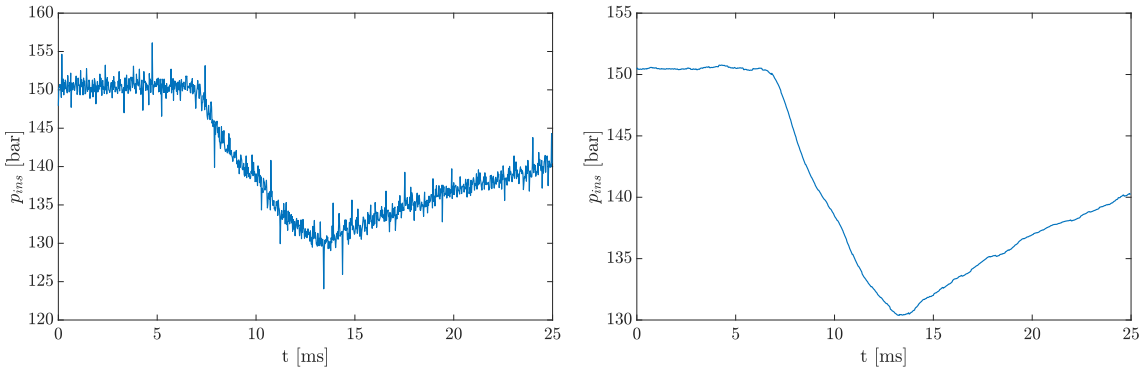

(a) Raw data of injection pressure (b) Processed injection pressure

Figure 5.5: Before and after processing of injection pressure

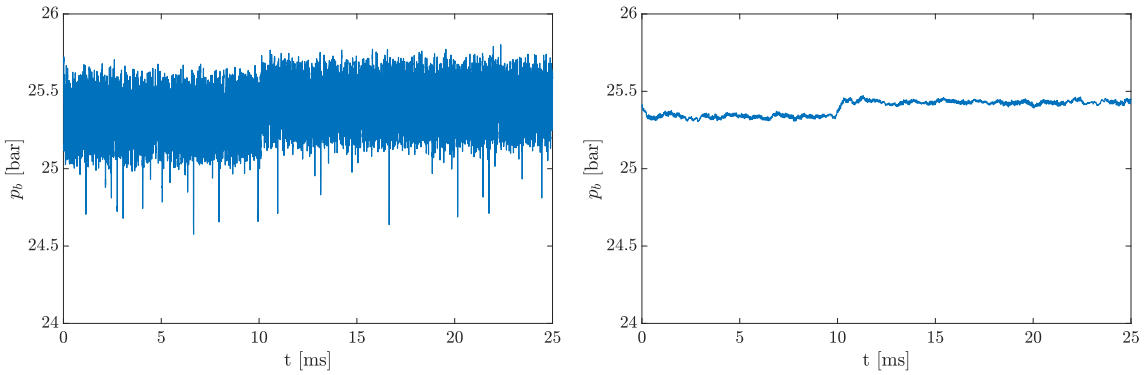

(a) Raw data of chamber pressure (b) Processed chamber pressure

Figure 5.6: Before and after processing of chamber pressure

After the MA was applied, the average of every experiment for each set was taken, then every calculation further was based on the average values.

5.2.2 Start and End Of Injection

In order to determine the start and end of injection, two different methods were used. The SOI was determined by the pressure gradient while EOI was determined by the minimum value of the pressure curve. In Figure 5.8 this is illustrated in addition to how they were used to establish the total injection time.

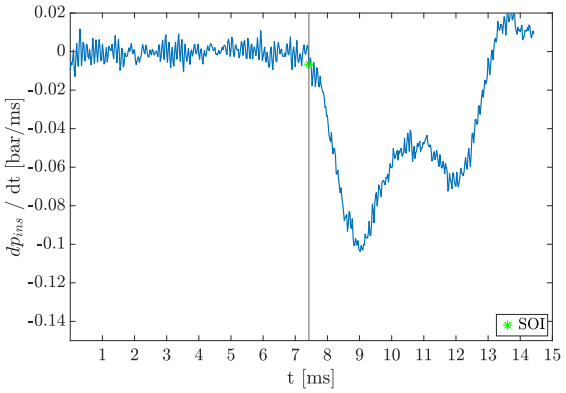

(a) Pressure gradient used for determining start of injection

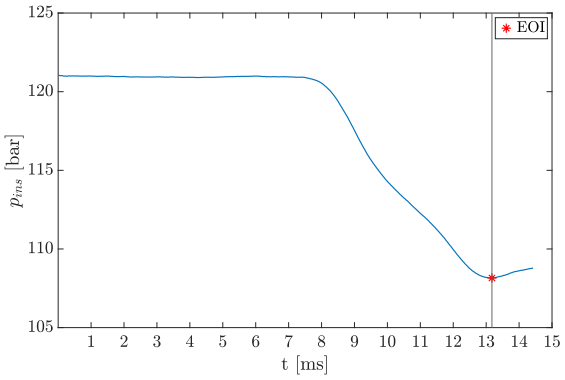

(b) Pressure curve used for determining end of injection

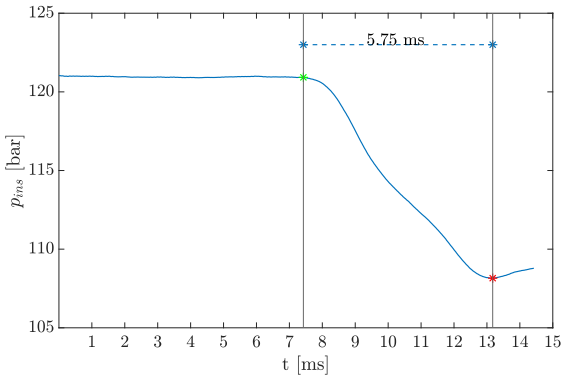

(c) Total injection time

Figure 5.7: Time of injection

By applying the MA to the pressure, it became possible to more accurately determine SOI by using the gradient of the pressure curve, illustrated in Figure 5.7a. The algorithm for determining SOI worked so that when the gradient of the present point and the 12 following points were negative, the present point was set to be where the injection began. Subsequently, EOI could not be determined by using the gradient because it was never strictly zero. Therefore, it was determined to be at the minimum value of the pressure curve as illustrated in Figure 5.7b. Where it was assumed that as soon as the needle closes, the pressure inside the injector will start to build back up. Figure 5.7c illustrates how both SOI and EOI were used to obtain the total injection duration.

This approach may lead to some inconsistencies when determining the SOI because the rate of pressure drop may vary dependent on the pressure. Thus the actual needle lift may occur slightly before any noticeable pressure drop. Also, the needle should lift at exactly the same time independently of the pressure. However, after further investigation, it was observed that the SOI varied by up to 0.8 ms for the different injection pressures.

5.2.3 Injection Delay

During the preliminary study it was discovered that the predetermined injection pulse length set in the control system, did not correspond with the actual injection length, as illustrated in Figure 5.7.

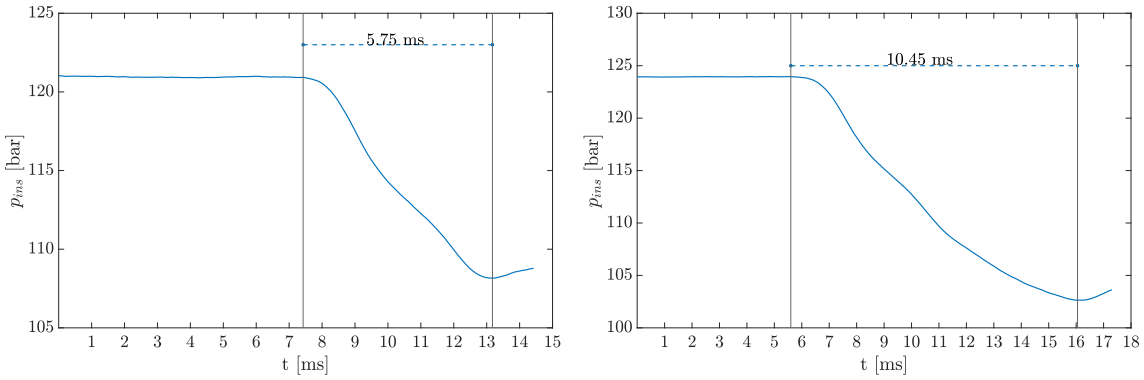

(a) Time of injection with a pulse length of 1 ms (b) Time of injection with a pulse length of 2 ms

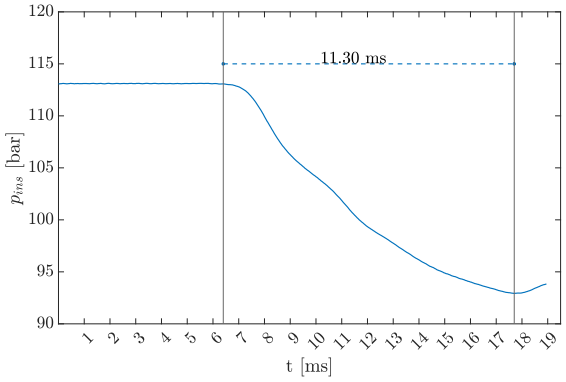

(c) Time of injection with a pulse length of 3 ms

Figure 5.8: Time of injection for different injection pulse lengths

When a signal of 1 ms was given, the injection time varied between 5-7 ms, while injection time increased significantly to approximately 10-11 and 11-12 ms for injection pulses of 2 and 3 ms, respectively. Based on this discovery, the injection pulse signal used in the experiments was set to 1 ms, which also was the lowest possible setting.

After the average values for each set were established with corresponding the SOI and EOI, it became possible to calculate the actual injection pressure for each set, the continuous nozzle pressure ratio and injection length, among others.

In previous studies with this setup, similar behavior has been observed and is believed to be caused by the inertial effects of the needle in the injector due to the slow dynamics of the hydraulic servo actuated injection valve (Myhrer, 2018) (Krivopolianskii, 2019).

Chapter 6

Results and Discussion

During the execution of the experiments, a total of thirty injections were conducted and recorded. Three different injection pressures were used, referred to as sets, where ten tests were performed for each of the sets at 80, 130 and 150 bar.

In order to reduce discrepancies and have a better foundation for predicting trends, the average values of every measurement in each set is presented.

6.1 Injector Dynamics

In an engine gaseous fuel may be injected from anywhere between 1-5 ms, dependent on the load of the engine. Hence this was also the aim when the experiments were conducted. However, as mentioned in subsection 5.2.3, that the actual injection time was much longer than the predetermined injection pulse, and consequently the injection pulse was set to 1 ms. The corresponding average injection length for each experiment is shown in Figure 6.1.

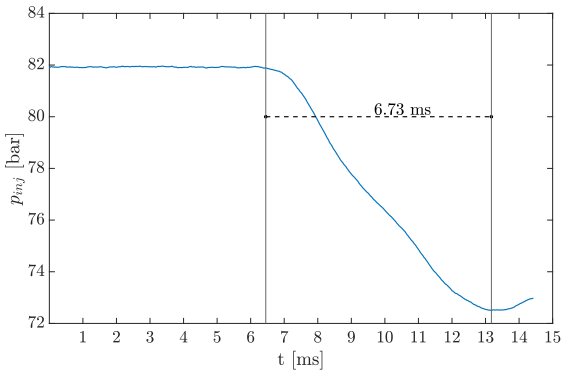

(a) Injection duration with injection pressure of 80 bar

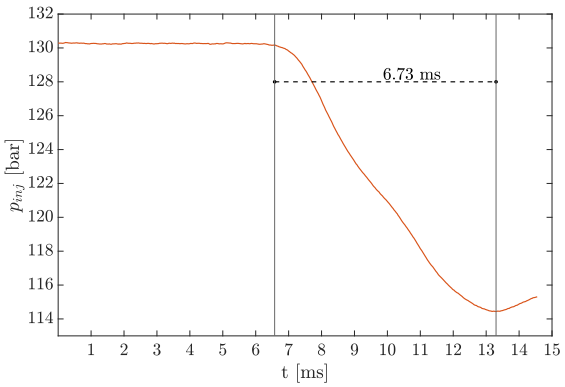

(b) Injection duration with injection pressure of 130 bar

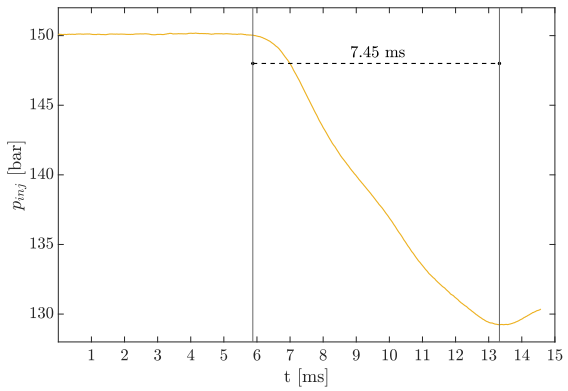

(c) Injection duration with injection pressure of 130 bar

Figure 6.1: Actual injection length for different injection time signals

From Figure 6.1 it is noticeable that there is a slight inconsistency in the SOI especially for $p_{inj} = 150$ bar compared with $p_{inj} = 130$ bar and $p_{inj} = 80$ bar. Figure 6.1c shows that SOI occurs slightly earlier compared with Figure 6.1a and Figure 6.1b. A reason for this might be due to the leak from the injector, which was noticeable at $p_{inj} = 150$ bar and not so much for the other injection pressures. Given that the gradient was used to determine the SOI, it is feasible that the pressure started to drop slightly before the others, where the leak was less prominent. Still, EOI occurred at approximately the same time for every injection varying with less than 0.15 ms on average at the most.

Additionally, there is a significant injection delay, independent of the injection pressure. There is a known delay in the control system, where the injection is initiated 250 μ after the measurements have started to log the data. However, that known delay only covers a fraction of the actual delay that is present in Figure 6.1. This fact does not pose any significant issues for further processing of the data. However, further figures using time as a scale will be presented with another time scale. Instead of using the total time, they are presented where SOI is zero, and the subsequent time will be the time after start of injection (t_{ASOI}).

One reason for the slow response of the injector might be due to the size of the needle. When looking at the technical drawing of the injector and needle geometry, attached in appendix A.1 A.2, it is clear that the needle runs through the entire injector. Meaning that the whole rod needs to be lifted during the injection.

6.2 Injection Pressure and Pressure drop

6.2.1 Total Pressure Drop

Among other things the injection pressure had a significant impact on the pressure drop over the injector, which can be seen in Figure 6.2, where the pressure drop for each experiment is shown. While the relative pressure drop stayed quite similar, varying by

approximately two percent at most seen in Table 6.1.

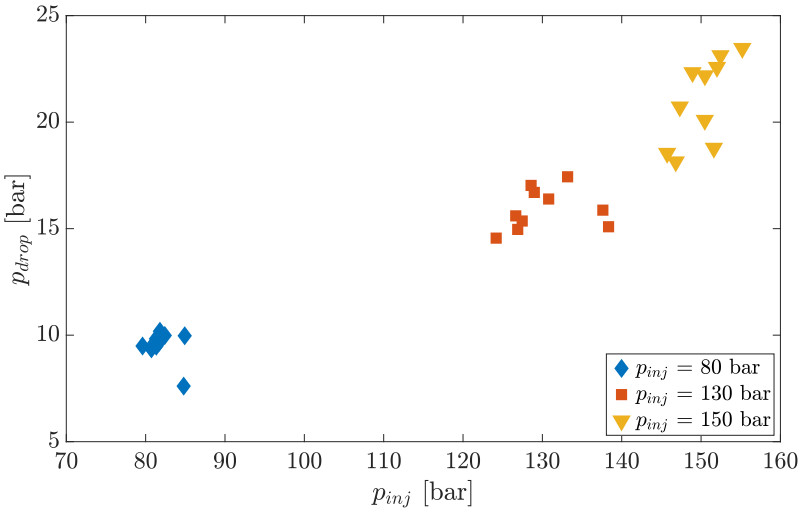

Figure 6.2: Pressure drop relative to injection pressure

The relative pressure drop is calculated using Equation 6.1 and was used to see how the pressure drop for the different injection pressures related to each other.

$$p_{drop,rel} = \frac{p_{drop}}{p_{inj}} \tag{6.1}$$

On average the total pressure drop were 9,4, 15,8 and 20.9 bar for injection pressures of 80, 130 and 150 bar, respectively.

Table 6.1: Dynamic pressure drop over injector. Where p_{inj} and p_{drop} are the average values for every test at each injection pressure. $p_{drop,max}$ and $p_{drop,min}$ are the maximum and minimum pressure drop for each injection pressure, while σ is the standard deviation for each set

p_{inj} [bar]	p_{drop} [bar]	$p_{drop,rel}$ [-]	$p_{drop,min}$ [bar]	$p_{drop,max}$ [bar]	σ_p [bar]
80	9.4	0.115	7.6	10.2	0.7
130	15.8	0.121	14.6	17.4	1.0
150	20.9	0.139	18.1	23.5	2.0

The observed deviation is primarily a consequence of that the injection pressure had to be regulated manually and for every injection. In combination with the severe leak from the injector, accurately controlling the pressure was challenging.

6.2.2 Continuous Pressure drop

In Figure 6.3 the instantaneous pressure drop, that is the dynamic pressure over the injector during the injection, for each injection pressure, is shown. During the first millisecond the pressure in the injector follows a curved line. Then the pressure drops more or less linearly until EOI, where the needle restricts the flow, and the pressure starts rising.

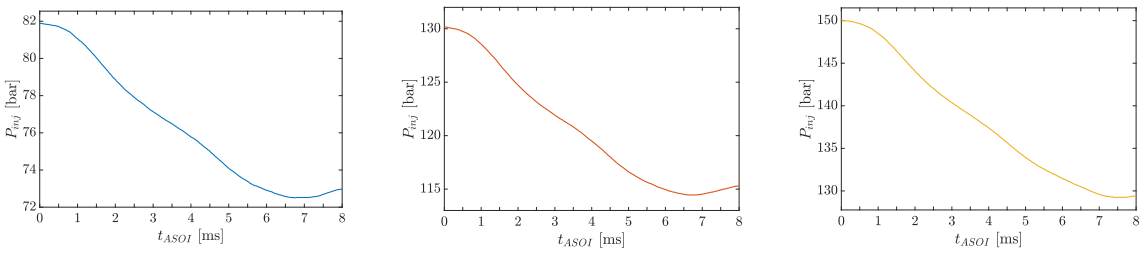

(a) 80 (b) 130 (c) 150

Figure 6.3: Instantaneous pressure curves

A prominent feature of the pressure curves is that they share a similar shape, independent of pressure. Figure 6.4 shows the dimensionless development of the instantaneous pressure in the injector against t_{ASOI}, where the y-axis is made dimensionless by dividing the instantaneous pressure by the injection pressure, while the x-axis is made dimensionless by dividing t_{ASOI} by the total injection time for each injection.

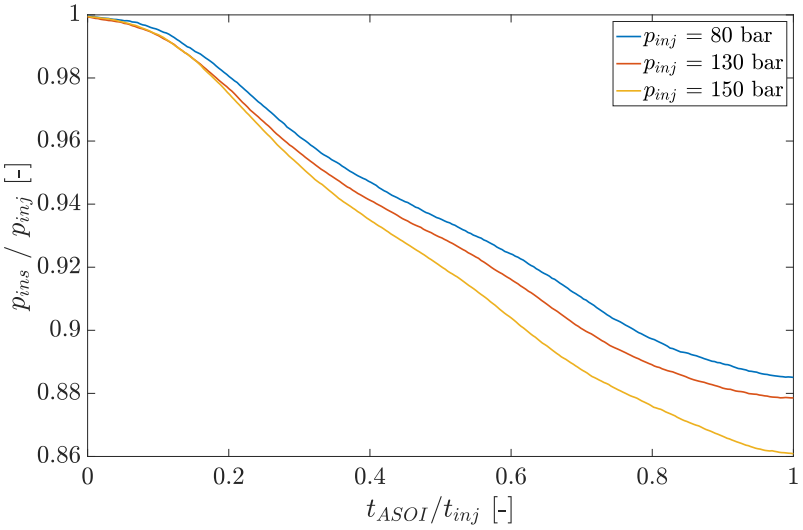

Figure 6.4: Normalized pressure curves

By normalizing the pressure drop, it becomes possible to visually express how the pressure drops relative to the injection pressure. As seen in Figure 6.4, the pressure develops almost identical initially. Thereafter the behavior of the dynamic pressures starts to deviate slightly. Still, the shape of the curves remain similar shape just with different magnitudes. The curve of a injection pressure of 150 bar seem to keep decreasing for a longer time than the other two. This might be caused by the leak.

6.3 Cone Angle

In Figure 6.5 the effect injection pressure has on cone angle is shown. The first frame is taken at 0.1 ms ASOI, because it was the first frame with a clear and visible jet.

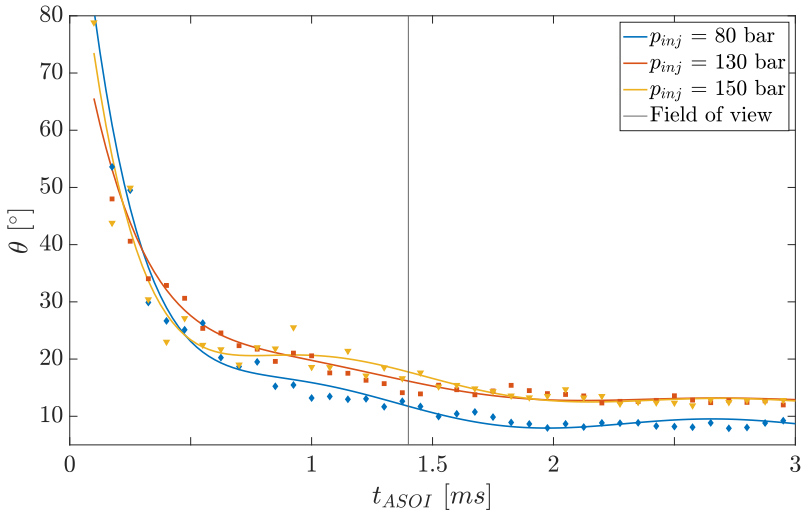

Figure 6.5: Development of cone angles for different injection pressures

Independent of injection pressure, the cone angle has a relatively high value just after SOI. There are two separate reasons for this phenomenon. Early in the injection stage, the jet has a relatively low velocity and thus also a low momentum. Therefore when it leaves the nozzle, due to the large pressure difference, it will expand in every direction also radially. Hence it develops a relatively wide penetration tip. Additionally, as mentioned previously in subsection 5.1.1, the cone angle is calculated from the center of the nozzle to the edges of the jet. Therefore, the nature of the script will provide a large cone angle for short jets, as illustrated in Figure 6.6a.

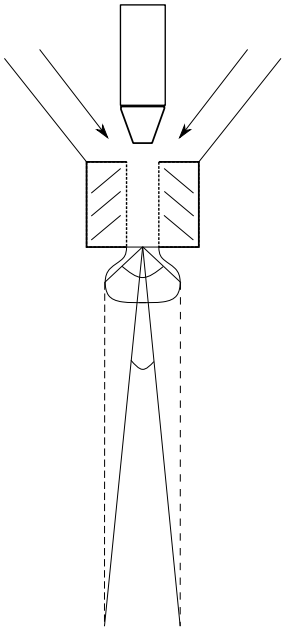

(a) Cross sectional sketch of nozzle, with initial expansion of the jet

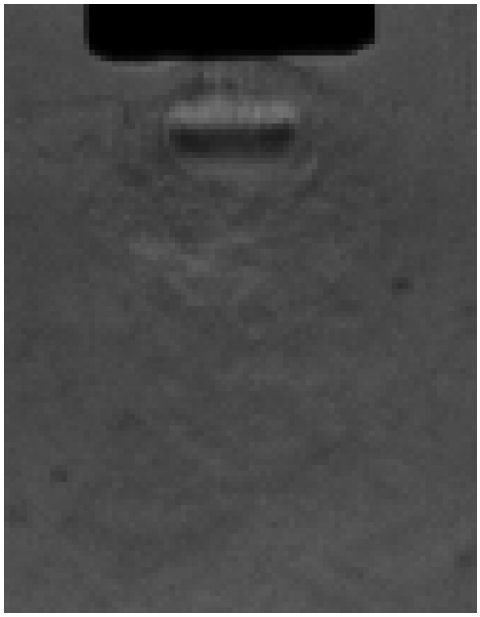

(b) Picture of jet showing initial expansion of the jet

Figure 6.6: Initial cone angle of jet

Figure 6.6a sketches the initial expansion of the jet. From the figure, it can be seen that a short jet will provide a much wider angle compared with a jet with the same diameter further downstream. Figure 6.6b shows a zoomed picture of the initial expansion of the jet.

An additional feature that might contribute to the initial large cone angle is the large volume in the nozzle. Due to the design of the nozzle, a bolt tightened to the end of the injector, a small volume, V_n inside the nozzle will experience the back pressure while the needle is closed, as illustrated in Figure 6.7.

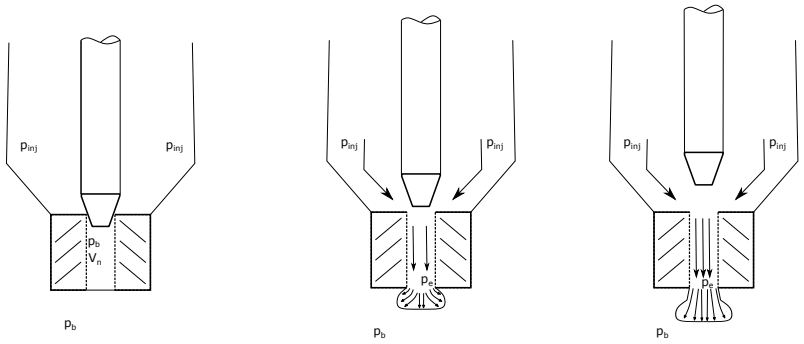

Figure 6.7: Nozzle Volume

As the needle start to lift, the small volume, V_n will be pushed out of the nozzle before the injected mass start to flow through the nozzle. As the needle continues to lift and the mass flow of the injected mass increases, thus also the momentum of the flow increases, and the jet gets pushed further out.

Still, the results show similar behavior as previous studies (Dong et al., 2018) (Yu et al., 2013). After the initial expansion of the jet, the cone angle decreases rapidly and reaches a relatively stable value after approximately 0.8 - 1.5 ms. This is because the momentum of the jet increases as the velocity increases. Due to the large momentum of the jet, it does not expand as much radially and is in a way pushed further out before it can spread and becomes fully developed.

However, there are some differences in how the jet behaves just before the stabilization period, between approximately 0.5 - 1 ms ASOI illustrated in Figure 6.8.

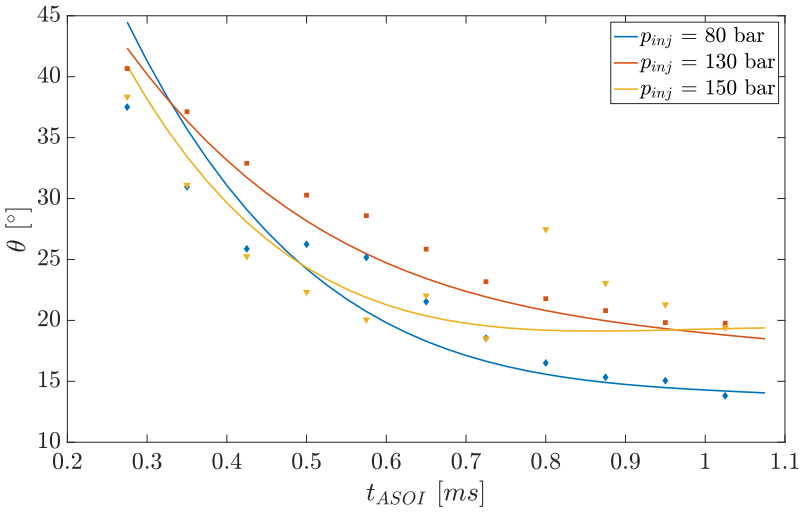

Figure 6.8: Cone angle between

The cone angle for the jets issued at p_{inj} = 80 and 150 bar, develops almost equal until 0.6 ms ASOI, where the angle of the jet at 150 bar starts to increase. On the other hand, the angle development for the jet injected at 130 bar deviates from the development of the two other jets in this time period. This phenomenon might at first appear as illogical or that an error has occurred. However, there might be a couple of reasons explaining this occurrence.

The various NPRs ended up at the limit of what is defined as moderately and highly underexpanded jets, because of the limitations imposed by the injector concerning injection pressure and leakage.

Referring to Figure 2.3 and Table 4.3, it is evident that the jet injected at 80 bar never becomes highly under expanded, hence the initial expansion of the jet will not have as large expansion-fan as the two others. Subsequently, the jet will not develop a wide initial jet boundary, which seems to influence the further development of the boundary. However, an injection pressure of 130 and 150 bar results in highly underexpanded jets, where a large NPR results in a more rapid expansion of the jet and a wider jet.

Still, if the same logic would be applied to the jets at 130 and 150 bar, it would be expected that the width of the jet issued with 150 bar should always be larger than the one at 130 bar, implying that the cone angle should be larger. By looking at Figure 6.9 it is clear

that the jet issued at 150 bar has a considerably larger nearfield jet width than the others, while the cone angle is smaller than the jet issued at 130 bar at that time.

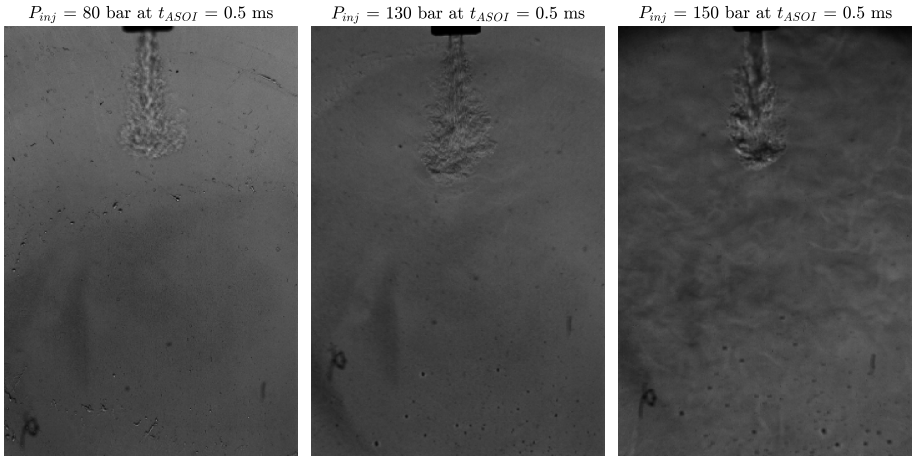

Figure 6.9: Picture of jets at $t_{ASOI} = 0.5$ ms

When looking at the images from this time period, it seems that the jet injected at 130 bar gets affected by the ambient sooner compared with the jet issued at 150 bar. This causes the jet to spread as regular turbulent motions dominate the jet tip. It appears that a higher injection pressure causes the core of the jet to propagate further before the ambient has an effect on the jet. This might be caused by the increased density of the injected mass due to the larger pressure. The jet at 80 bar has also started to develop a turbulent penetration tip, but the narrow near nozzle width is small, causing the angle of the jet to be small.

6.3.1 Relation of Cone Angle and Pressure

An interesting observation that can be made from the pressure drop over the injector and the development of the cone angle, is that both curves appear nonlinear simultaneously and as the pressure drops become more linear, so does the development of the cone angle, illustrated in Figure 6.10.

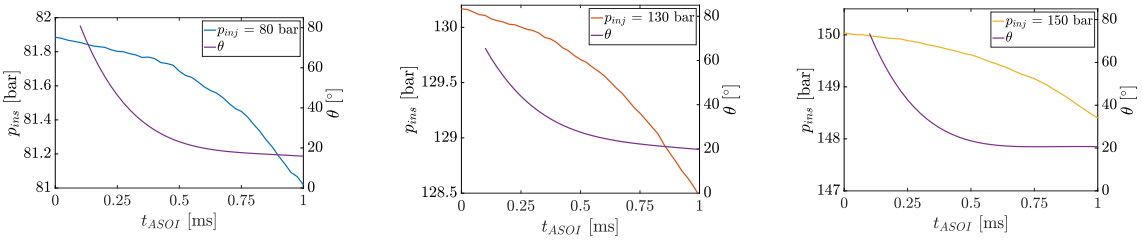

(a) p_{ins} curves and θ for p_{inj} = 80 bar

(b) p_{ins} curves and θ for p_{inj} = 130 bar

(c) p_{ins} curves and θ for p_{inj} = 150 bar

Figure 6.10: Instantaneous pressure curves and cone angles

However, the connection between them is difficult to extract. The pressure is more or less

constant during this period, considering that it drops with less than 1 % of the injection pressures independent of the magnitude of the pressure. Given that many other external factors influence the jet and cone angle, a direct connection to the dynamic pressure over the injector is less obvious.

While the injection pressure has a effect on the cone angle in general, there is no obvious connection between the instantaneous pressure drop and how the cone angle develops.

6.4 Penetration Length

The jet tip penetration is a crucial aspect with respect to air utilization and fuel-air mixing. A longer jet will increase the jet volume and consequently affect the formation and distribution of the mixture (Yu et al., 2013).

Due to limited access to optical equipment, the area of the chamber that could be captured with the camera was restricted. As a consequence, only about two-thirds of the chamber was captured, corresponding to approximately 60 mm from nozzle tip to the edge of each frame. Hence the penetration length became restricted by the field of view.

Figure 6.11 shows how the penetration tip propagates and displays the development until the penetration tip passes the captured area, at approximately 1.1 - 1.4 ms ASOI.

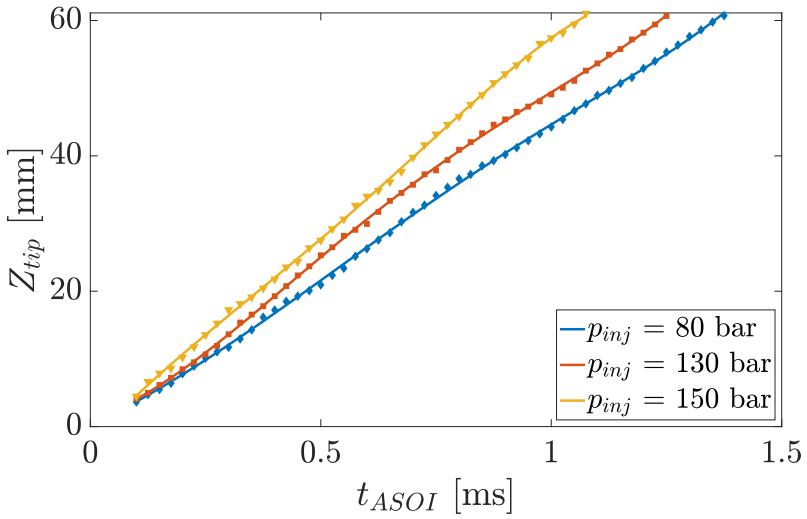

Figure 6.11: Jet penetration tip propagation length

From Figure 6.11, it can be observed that the penetration length develops similar independent of injection pressure. Higher injection pressure corresponds to a slightly faster jet penetration development. In addition, Z_{tip} propagates close to linear for the sampling area.

Considering that the characteristics in the farfield region are significantly different from the nearfield, in the sense that the jet has fully expanded and the properties of the flow are self-similar. Aerodynamic drag is expected to affect the development of the tip as

the surface area increases. The extra drag is expected to slow down the development of the jet. Although the curve for the penetration tip starts to curve slightly, the drag does not seem to have a significant effect, causing the results obtained here to deviate from previous studies (White and Milton, 2008) (Yu et al., 2013). One reason might be the significantly larger nozzle diameter used in this study compared to those used in White and Milton (2008) and Yu et al. (2013), which was six 0.2 mm holes and a 1.4mm hole for the respective studies and a 2.04 mm in this study.

Another reason for drag not having a noticeable influence on the penetration tip might be due to the limited area that was captured with the camera. The drag might have more of an impact on the tip after it has passed the captured area.

6.4.1 Penetration Length and Pressure

Initially, the linear behavior of the tip penetration tip seems illogical. However, the pressure drop during the development of the jet was less than 1% of the injection pressure. Meaning that the nozzle pressure was kept above the critical pressure, which ensured that the flow was choked and mass flow constant during the development of the jet. The continuous pressure over the injector, together with the development of the penetration tip, can be seen in Figure 6.12.

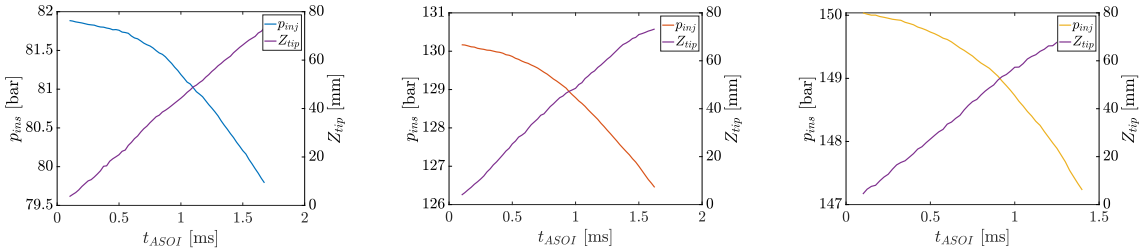

(a) p_{ins} curves and θ for p_{inj} = 80 bar

(b) p_{ins} curves and θ for p_{inj} = 130 bar

(c) p_{ins} curves and θ for p_{inj} = 150 bar

Figure 6.12: Pressure vs penetration length

As for the development of the cone angle, it is not clear how the instantaneous pressure affects the penetration tip. Because the captured area is restricted, the pressure remains close to constant during the sampling period such that the initial condition for the jet is not changing during the development.

6.4.2 Jet Tip Velocity

The jet tip velocity can provide useful information on how the penetration tip develops. The propagation velocity can be directly computed from the development of the penetration length. Figure 6.13 illustrates the evolution of the velocity for the different injection pressures with respect to time.

Referring to section 5.1, minor relative differences in penetration lengths significantly impacted the associated velocity during the unsteady development of the penetration tip.

The sensitivity to small changes and the rapid changes of the jet from frame to frame causes a large variance in the calculated velocity.

Due to this sensitivity, the velocity was calculated using a larger step size of 0.05 ms to reduce the effect of the sensitivity. Additionally, a moving average has been applied to decrease the large variance.

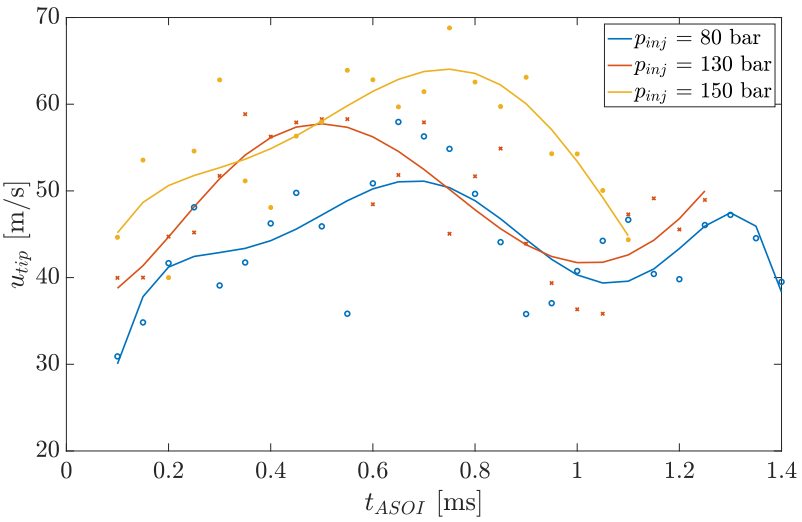

Figure 6.13: Jet penetration tip velocity

Independent of injection pressure, the jets undergo an initial acceleration for the first 0.5 - 0.8 ms of the injection. The jet issued at 150 bar has a larger initial velocity than those issued at lower pressures. However, the acceleration is slightly below the jet issued at 130 bar, while the velocity develops similarly to the jet issued at 80 bar.

The shape of the velocity curves might be related to the cone angle of the jet. Referring to the discussion of Figure 6.8 and 6.9 in section 6.3, the cone angles of the jet issued at 80 and 150 bar develop similar up to approximately 0.6 ms ASOI and that the jet issued at 130 bar gets affected by the ambient sooner than the jet issued at 150 bar. Together with that, a larger cone angle implies a wider jet. The fact that the ambient affects the penetration tip sooner for the jet issued at 130 bar can explain why the velocity of the associated jet to decelerate sooner than the other two. Because the jet is wider, the force of the drag from the ambient will also be larger, causing the jet to slow down. Additionally, it was observed that the jet issued at 150 bar had a wider near field structure, which might explain the relatively low acceleration it experiences.

Generally a higher leads to a larger tip velocity, this will probably be the case up to a certain value of NPR. Previous studies have shown that for NPR $>$ 10 the velocity at for the initial propagation do not increase further (Yu et al., 2013).

6.5 Visual Inspection of Jet

The images provide other interesting nearfield jet characteristics such as the development of Mach disks and shock structures. In addition, the transition stages the jet goes through during the injection.

However, the developed post-processing script was unable to determine such effects. Hence they are presented and discussed by the images themselves.

6.5.1 Jet development for a Injection Pressure of 80 bar

Figure 6.14 shows a picture sequence, from 0.15 to 2 ms ASOI, of how the jet develops with a injection pressure of 80 bar.

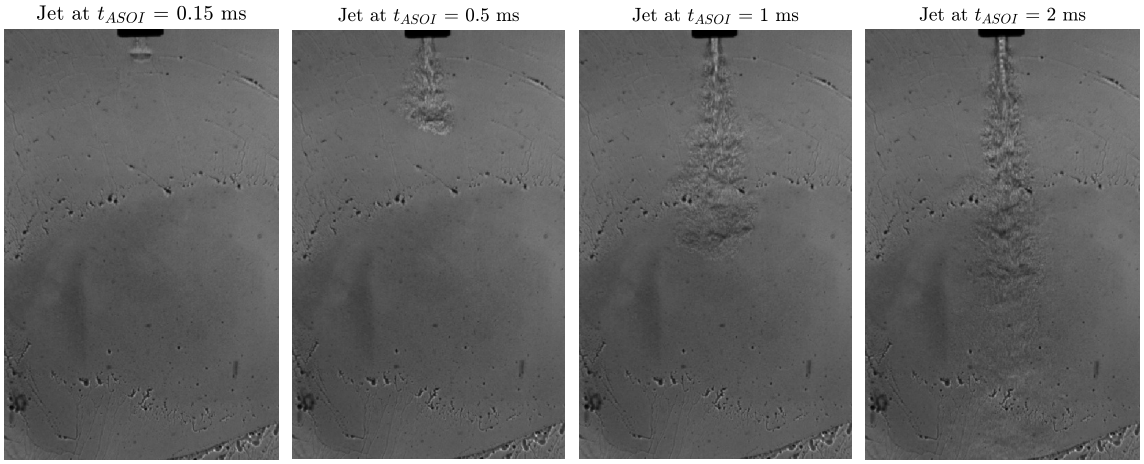

Figure 6.14: Picture sequence of jet issued at 80 bar

The initial expansion of the nozzle volume, discussed in section 6.3, can still be seen intact after 0.15 ms however, it has been pushed further downstream. After 0.5 ms, the tip of the jet starts to be affected by the ambient and the penetration tip starts to become turbulent. At 1 ms ASOI, the core of the jet is turning visible, indicating that initial shock structures are developing. The shock cells have become even more visible after 2 ms, given that the pressure at this point has dropped slightly, to approximately 78 bar, the effective NPR is 2.9, and consequently, the jet can be characterized as moderately underexpanded. Therefore the jet never develops the shock structures of a highly underexpanded jet and the Mach disk will not appear.

When the core of the jet has become stationary, at 2 ms ASOI, the width one nozzle width downstream is approximately 2.5 mm. Indicating a small expansion from the nozzle that has a width of 2.04 mm.

6.5.2 Jet development for a Injection Pressure of 130 bar

Figure 6.15 shows a time series of the jet development from t_{ASOI} ranging from 0.15 to 2 ms and $p_{inj} = 130$ bar.

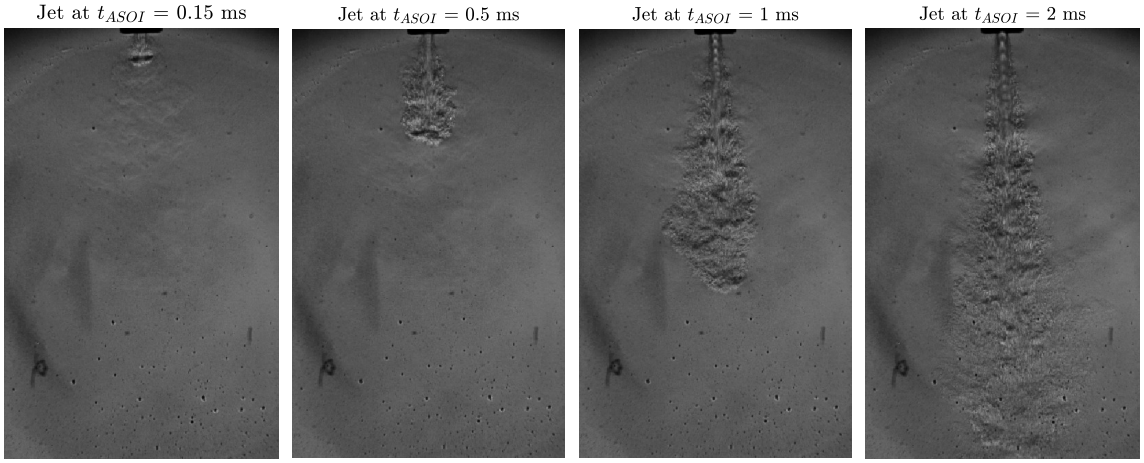

Figure 6.15: Picture sequence of jet issued at 130 bar

From Figure 6.15, it can be observed that the initial expansion of the jet is also visible with 130 bar of injection pressure. However, it has disintegrated more than compared with Figure 6.14. Further, at approximately $t_{ASOI} = 0.5$ ms, the jet appears to transition from subsonic to moderately underexpanded. Additionally, the penetration tip is beginning to be influenced by the ambient in this region.

At $t_{ASOI} = 1$ ms, the jet has transitioned to the moderately underexpanded stage and shock structures are clearly visible. However, the core is still increasing in size and a normal shock is not yet visible.

After 2 ms, the core of the jet has become stationary, and the initial shock can be described as having a bell-like shape. When looked at more closely, the bell does not coalesce at the center line of the jet. At the end of the first shock cell, the Mach disk can be seen as a horizontal straight black line in the reference picture. When the jet has become fully developed, the width of the jet, one nozzle width downstream, is approximately 2.9 mm. Compared with the width of the jet injected at 80 bar, this is a 0.4 mm increase of the width. Meaning that for a distance of just 2 mm, which is the nozzle width, the jet has expanded significantly more.

6.5.3 Jet development for a Injection Pressure of 150 bar

Figure 6.16 illustrates the development of the jet for the same time period that is discussed in the two preceding sections.

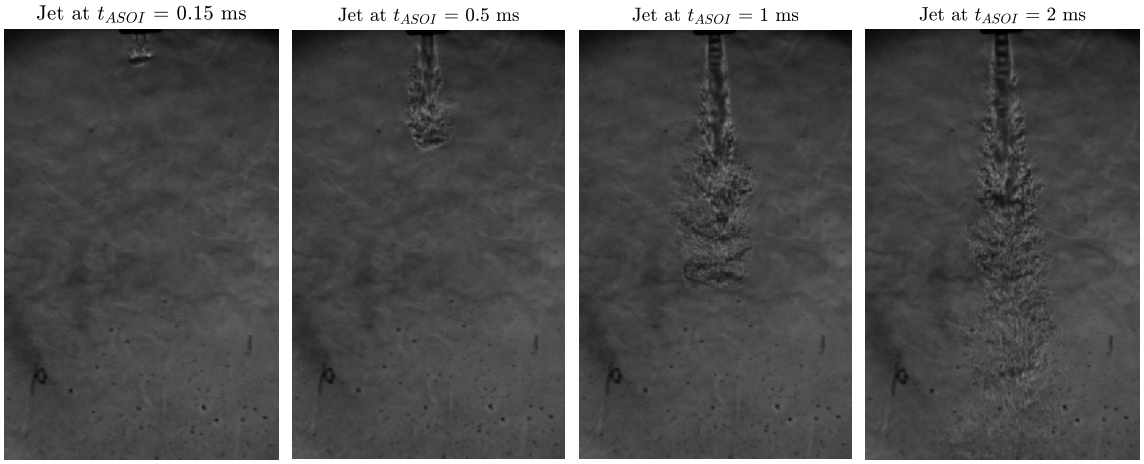

Figure 6.16: Picture sequence of jet issued at 150 bar

The initial expansion of the jet volume can be observed to have disintegrated further and the jet has started to pass through it. After 0.5 ms, the jet has developed a significantly wider core that additionally seems to penetrate further before the surroundings influence the tip. After 1 ms, the core of the jet has become extremely dark compared with the other injection pressures, which makes it difficult to detect the shock structures. Still, periodically brighter sections can be observed, indicating local changes in density and, consequently, pressure. These changes in pressure are related to the presence of shock structures in the jet due to underexpansion.

When the jet has become fully developed, the width of the jet, one nozzle width downstream, is approximately 3.5 mm, indicating an even larger expansion angle than the lower injection pressures.

6.5.4 Near Field Region of Stationary Jet

Due to the limited field of view, the effect the pressure drop has on the jet structure in the farfield region, is difficult to determine. However, the nearfield region is possible to investigate. Figure 6.17 shows the jet issued at different injection pressures, for when it is fully developed between 2 and 4 ms ASOI. In addition, the instantaneous pressures are indicated above each picture.

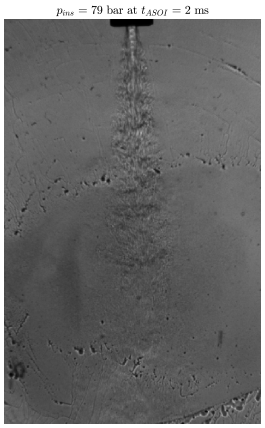

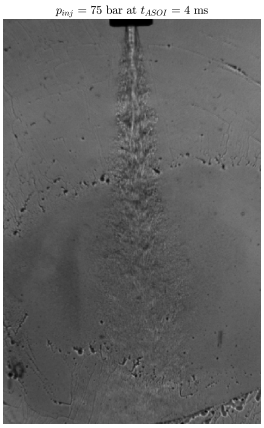

(a) Pictures of jet issued at 800 bar between 2 and 4 ms

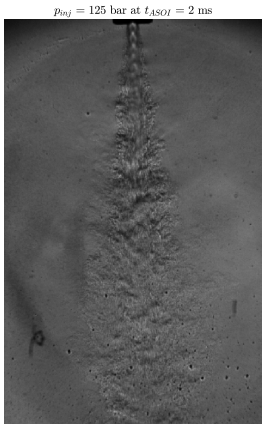

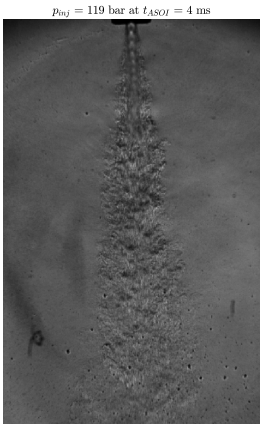

(b) Pictures of jet issued at 130 bar between 2 and 4 ms

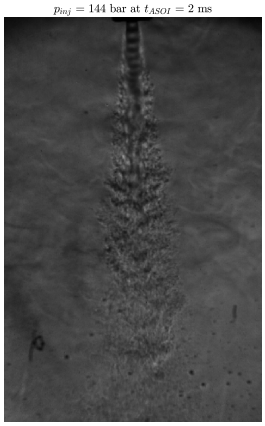

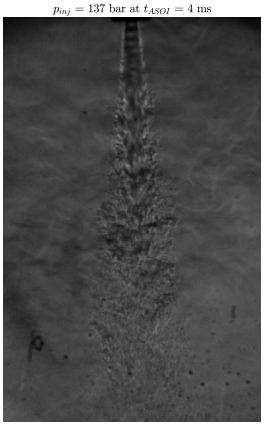

(c) Pictures of jet issued at 150 bar between 2 and 4 ms

Figure 6.17: Nearfield region of jets

Even though the total pressure drop for the individual injection pressures are different from each other, the relative pressure drop remains more or less equal in the time interval at approximately 5 %, shown in Table 6.2.

Table 6.2: Pressure drop for fully developed jet. $p_{drop,rel}$ is the relative pressure drop between $p_{ins(2ms)}$ and $p_{ins(4ms)}$

p_{inj} [bar]	p_{ins}(2 ms) [bar]	p_{ins}(4 ms) [bar]	$p_{drop,rel}$ [-]
80	79	75	0.051
130	125	119	0.048
150	144	137	0.049

From Figure 6.17, there are no apparent differences in the appearance of the nearfield structure in either of the jets. However, a decrease in pressure should result in a smaller expansion angle, meaning that the diameter of the jet should be more narrow at 4 ms ASOI than it is after 2 ms. However, the pressure differences are too small for an observable change in the jet width at this resolution. The difference might be more evident later in

the injection stage, when the pressure difference has increased further. However, in this study, only 4 ms of the injection was captured optically, making it infeasible to investigate that relation further.

Chapter 7

Conclusion and Further Works

Due to the increased attention regarding emissions and pollutants in the shipping industry, a lot of attention and effort have been aimed at finding new, more energy-efficient and environmentally friendly alternative solutions.

Among the proposed solutions, LNG has emerged as a favorable alternative fuel due to the significant reduction of emissions of interest, such as CO_2, NO_X, SO_X and particulate matter. Additionally, some engine using LNG as fuel has obtained efficiencies as high as 48 %.

Even though LNG has many advantages, it also has its set of challenges. Gas engines where LNG is injected at low pressures, suffer from methane slip into the exhaust, that is unburned methane from the LNG that escapes through the exhaust and into the atmosphere. To address this issue, an engine design where gas is direct injected at high pressures has been developed. However, due to the compressible nature of gaseous fluids at high pressures, the pressure over the injector will drop significantly during the course of the injection.

This study has presented the results of experiments conducted using a constant volume combustion chamber, where three different injection pressures, of 80, 130 and 150 bar, have been used to inject nitrogen into an ambient with a density of 28 kg/m^3. The aim was to study the effect injection pressure has on jet development, where the pressure over the injector was measured at a sampling frequency of 40 kHz.

7.1 Summary of Results

7.1.1 Dynamic Pressure Drop

Generally, a larger injection pressure leads to a larger and faster total pressure drop over the injector, while the relative pressure drop is kept more or less equal everything else kept equal Table 6.1. For a given nozzle geometry, the pressure seems to behave similarly, meaning that independent of injection pressure, the pressure drops similarly, with a

different magnitude.

The injection pressure affects the NPR, where an increase in injection pressure will increase the NPR, when the back pressure is kept constant. For the experiments conducted in this study, the only variable was the injection pressure, hence a change in injection pressure corresponds to a proportional change in NPR.

7.1.2 Cone Angle

During the initial phase of the jet development, the angle maintained a relatively large value independent of injection pressure before decreasing rapidly. This was believed to be caused mainly by low initial momentum and how the cone angle was calculated. Another possible large initial cone angle may be related to the nozzle volume.

During the initial stage of the injection, to approximately 0.5 ms ASOI, NPR had a seemingly small effect on the cone angle of the jet. However, when shock cells were developed, the angle of the jets started to deviate based on the injection pressure. When the jets had a clear near- and farfield region, approximately between 1 - 2 ms, a larger injection pressure resulted in a larger cone angle.

An injection pressure of 80 bar corresponds to a NPR of 3.2 at SOI, meaning that the jet never becomes highly underexpanded. In turn, this will cause the jet to not expands as wide as the other two jets that were issued at pressures resulting in highly underexpanded jets. Due to the low expansion, the jet issued at 80 bar developed a smaller angle.

An injection pressure of 150 bar, resulted in an initially smaller angle than the jet issued at 130 bar, before it later became larger. One reason might be that a larger density, of the injected mass, causes the jet to penetrate further before the ambient influences it. Such that the jet penetrates further before the ambient influences the penetration tip.

On the other hand, the instantaneous pressure drop over the injector did not have any observed effect on the cone angle. First, this was because the area that was captured of the chamber was limited to approximately two-thirds of the chamber. Hence, it was no longer possible to accurately determine the angle when the jet passed the field of view, after between 1.1 and 1.4 ms ASOI. Additionally, the pressure drop during this time period was negligible.

7.1.3 Penetration Length and Velocity

Independent of the injection pressure, the jets develop similarly, however at slightly different rates. As previously mentioned, approximately two-thirds of the chamber was captured by the camera, thus limiting how much of the jet that was captured. Nonetheless, the jet tip seems to develop rather linear, which contradicts other studies, where the initial development is linear but quickly turns nonlinear as the drag from the ambient slows the jet down (Yu et al., 2013).

When looking at the velocity of the jet, it is clearly undergoing an initial acceleration before a slight stabilization period, followed by a noticeable decrease in velocity. This is directly correlated with the drag by the ambient on the penetration tip. Generally, a larger injection pressure results in a larger velocity of the penetration tip.

The developed post-processing script was very sensitive to relative differences in the length between two time steps, for smaller time steps. It resulted in a significant variance between each time step of the velocity.

As for the cone angle, it is difficult to say if the instantaneous pressure drop influenced the penetration tip length and velocity. As the total pressure drop during the sampling period was negligible, such that the initial condition during the development was close to constant.

7.1.4 Visual Inspection of Jet Development

A larger NPR corresponded to a more distinct shock structure and a wider core of the jet. Previous studies have also concluded that a large NPR will increase the jet nearfield region angle, which in turn promotes spatial distribution and mixing of the jet (Dong et al., 2018) (Yu et al., 2013).

For the highly underexpanded jets, i.e. p_{inj} = 130 bar and p_{inj} = 150 bar, the ambient seems to influence the jet later for a larger NPR, which causes the jet to penetrate further before it equalizes the ambient back pressure, and develops a self-similar jet tip.

The total sampling period of images was 4 ms, hence it was possible to analyze the near field region of the jet for a more extended time period than the cone angle, penetration- tip and velocity. The jets were analyzed when they were fully developed from 2-4 ms ASOI. During this sampling period, the gauged pressure drop was ranging from 4, 6 and 7 bar for injection pressures of 80, 130 and 150 bar, respectively.

However, for the given resolution of the pictures, there was no visible change related to the width or shock structure of the jet.

7.2 Suggestions for Further Works

This thesis has tried to quantify the effect of dynamic pressure drop for gaseous fuel injection and observe its effect on the physical characteristics of the issued jet. As discussed previously, although the injection pressure impacted the jet structure, in this study, the instantaneous pressure drop had close to no effect on cone angle, penetration length, shock structure or near field jet width. However, several limiting factors can be eliminated to have a better basis for this claim. These factors include other aspects that could be focused on and improvements to the experimental setup.

7.2.1 Suggestions for Further Experimental Study

This study has concluded that there was no connection between the dynamic pressure drop and the characteristic features of the injected gas jet. However, some aspects could be improved to more definitely state this.

First and foremost, it should be ensured that the entire injection is captured by the camera. Both in terms of duration and that the whole chamber is visible in each frame.

Additionally, experiments focused on the near field region of the jet could be conducted to more accurately determine the shock structures in the jet.

For more accurate properties of the injected medium, it should be considered to inject methane instead of nitrogen. Subsequently, necessary safety measures must be taken into account.

Also, it can be considered to inject for a longer time period in order to get a significant pressure drop to see when there is a clear and visible change in jet structure.

7.2.2 Suggestions for Improvement of Experimental Set Up

Given that the setup used in this thesis will be dissembled, moved to a different location and rebuilt, some suggestions for aspects to be considered are included. First, the injector must either be redesigned to prevent leaks or replaced by an industry made injector. It should also be considered to design a mutual arrangement for gas and diesel injections to investigate reacting jets. The current control of injection pressure is not very accurate and makes it difficult to control the injection pressure. Hence, a study on an alternative compression and control sequence would be beneficial.

Additionally, the optical lenses used for this setup were too small. The diameter of the lens was too small relative to the diameter of the chamber's windows. In order to fully illuminate the chamber, it should be considered to go for the procurement of larger lenses. Additionally, a more thorough investigation for optimal camera lens should be conducted.

The structure and documentation of the LabView control system are not satisfactory and cumbersome to get acquainted with. It should be removed and done all over according to industry standards. Additionally, a system where changes are documented should be implemented in order for others to quickly get an overview of the setup. An additional suggestion would be for the users of the rig to take a course on how to develop LabView scripts properly.

Bibliography

Æsøy, Vilmar, Einang, Per Magne, Stenersen, Dag, Hennie, Erik and Valberg, Ingebrigt (2011) LNG-Fuelled Engines and Fuel Systems for Medium Speed Engines in Maritime Applications, *SAE International*. ISSN: 0148-7191. DOI: https://doi.org/10.4271/2011-01-1998.

Ahmad, Zeeshan, Kaario, Ossi, Qiang, Cheng and Larmi, Martti (2021) Effect of pilot fuel properties on lean dual-fuel combustion and emission characteristics in a heavy-duty engine, *Applied Energy*, 282, p. 116134. ISSN: 0306-2619. DOI: https://doi.org/10.1016/j.apenergy.2020.116134. Available at: https://www.sciencedirect.com/science/article/pii/S030626192031549X.

Anderson Jr., John D (2003) *Modern Compressible Flow With Historical Perspective*. 3rd ed. New York: McGraw-Hill.

Corbett, James J., Winebrake, James J., Green, Erin H., Kasibhatla, Prasad, Eyring, Veronika and Lauer, Axel (2007) Mortality from Ship Emissions: A Global Assessment, *Environmental Science & Technology*, 41(24), pp. 8512–8518. DOI: 10.1021/es071686z.

CRIST, S., GLASS, D. R. and Sherman, P. M. (2012) Study of the Highly Underexpanded Sonic Jet, *AIAA*, 4(1). DOI: 10.2514/3.3386.

Donaldson, Coleman duP. and Snedeker, Richard S. (1971) A study of free jet impingement. Part 1. Mean properties of free and impinging jets, *Journal of Fluid Mechanics*, 45(2), pp. 281–319. DOI: 10.1017/S0022112071000053.

Dong, Quan, Li, Yue, Song, Enzhe, Fan, Liyun, Yao, Chong and Sun, Jun (2018) Visualization research on injection characteristics of high-pressure gas jets for natural gas engine, *Applied Thermal Engineering*, 132, pp. 165–173. ISSN: 1359-4311. DOI: https://doi.org/10.1016/j.applthermaleng.2017.12.093. Available at: https://www.sciencedirect.com/science/article/pii/S1359431117337997.

Dong, Quan, Li, Yue, Song, Enzhe, Yao, Chong, Fan, Liyun and Sun, Jun (2017) The characteristic analysis of high-pressure gas jets for natural gas engine based on shock

wave structure, *Energy Conversion and Management*, 149, pp. 26–38. ISSN: 0196-8904. DOI: https://doi.org/10.1016/j.enconman.2017.06.015. Available at: https://www.sciencedirect.com/science/article/pii/S0196890417305587.

Franquet, Erwin, Perrier, Vincent, Gibout, Stéphane and Bruel, Pascal (2015) Free underexpanded jets in a quiescent medium: A review, *Progress in Aerospace Sciences*, 77, pp. 25–53. ISSN: 0376-0421. DOI: https://doi.org/10.1016/j.paerosci.2015.06.006. Available at: https://www.sciencedirect.com/science/article/pii/S0376042115000548.

Golub, V.V., Baklanov, D.I., Bazhenova, T.V., Bragin, M.V., Golovastov, S.V., Ivanov, M.F. and Volodin, V.V. (2007) Shock-induced ignition of hydrogen gas during accidental or technical opening of high-pressure tanks, *Journal of Loss Prevention in the Process Industries*, 20(4). Selected Papers Presented at the Sixth International Symposium on Hazards, Prevention and Mitigation of Industrial Explosions, pp. 439–446. ISSN: 0950-4230. DOI: doi.org/10.1016/j.jlp.2007.03.014.

GRAUR, I. A., ELIZAROVA, T. G., RAMOS, A., TEJEDA, G., FERNÁNDEZ, J. M. and MONTERO, S. (2004) A study of shock waves in expanding flows on the basis of spectroscopic experiments and quasi-gasdynamic equations, *Journal of Fluid Mechanics*, 504, pp. 239–270. DOI: 10.1017/S0022112004008274.

Haji, Alireza, Edgington-Mitchell, Daniel, Honnery, Damon, Montazerin, Nader, Abdullah, Amir and Mirsalim, Seyed (Nov. 2016) Ultra high speed investigation of gaseous jet injected by a single-hole injector and proposing of an analytical method for pressure loss prediction during transient injection, *Fuel*, 184, pp. 100–109. DOI: 10.1016/j.fuel.2016.06.112.

Hamzehloo, A. and Aleiferis, P.G. (2016) Gas dynamics and flow characteristics of highly turbulent under-expanded hydrogen and methane jets under various nozzle pressure ratios and ambient pressures, *International Journal of Hydrogen Energy*, 41(15), pp. 6544–6566. ISSN: 0360-3199. DOI: https://doi.org/10.1016/j.ijhydene.2016.02.017. Available at: https://www.sciencedirect.com/science/article/pii/S0360319915316669.

Heywood, John B. (2018) *Internal Combustion Engine Fundamentals*. 2nd ed. New York: McGraw -Hill Education.

Hill, Philip G. and Ouellette, Patric (Mar. 1999) Transient Turbulent Gaseous Fuel Jets for Diesel Engines, *Journal of Fluids Engineering*, 121(1), pp. 93–101. ISSN: 0098-2202. DOI: 10.1115/1.2822018. Available at: https://doi.org/10.1115/1.2822018.

International Maritime Organization (2022) *Fourth Greenhouse Gas Study 2020*. Available at: https://www.imo.org/en/OurWork/Environment/Pages/Fourth-IMO-Greenhouse-Gas-Study-2020.aspx (Accessed: 2nd Aug. 2022).

Krivopolianskii, Vladimir (2019) Experimental investigation of injection and combustion processes in marine gas engines using constant volume rig,

Moran, Shapiro, Boettner and Baily (2015) *Principle of Engineering Thermodynamics*. Wiley. DOI: 978-1-118-96088-2.

Munday, D., Gutmark, E., Liu, J. and Kailasanath, K. (2011) Flow structure and acoustics of supersonic jets from conical convergent-divergent nozzles, *Physics of Fluids*, 23(11), p. 116102. DOI: 10.1063/1.3657824.

Myhrer, Bredahl Jens Kristian (2018) *Experimental Study of High-Pressure Gas Injection Using Optical Methods*, Master thesis, Available at: http://hdl.handle.net/11250/2564510 (Accessed: 23rd May 2022).

Nelin, T.D., Joseph, A. M., Gorr, M.W. and Wold, L.E. (2012) Direct and Indirect Effects of PM on the Cardiovascular System, *Toxicology letters*, 208(3), pp. 293–299. DOI: 10.1016/j.toxlet.2011.11.008. Available at: https://www.ncbi.nlm.nih.gov/pmc/articles/PMC3248967/.

Otsu, Nobuyuki (1979) A Tlreshold Selection Method from Gray-Level Histograms, *IEEE*, 9, pp. 62–66. Available at: https://ieeexplore.ieee.org/stamp/stamp.jsp?tp=&arnumber=4310076.

Settles, G.S. (2001) *Schlieren and Shadowgraph Techniques: visualizing phenomena in transparent media*. 1st ed. Berlin: Springer. DOI: 10.1007/978-3-642-56640-0.

Sezgin, Mehmet and Sankur, Bülent (2014) Survey over image thresholding techniques and quantitative performance evaluation, *Journal of Electronic Imaging*, 13. DOI: 10.1117/1.1631315. Available at: https://www.spiedigitallibrary.org/journals/journal-of-electronic-imaging/volume-13/issue-01/0000/Survey-over-image-thresholding-techniques-and-quantitative-performance-evaluation/10.1117/1.1631315.full?SSO=1.

Stenersen, Dag and Thonstad, Ole (2017) *GHG and NOx emissions from gas fuelled engines*. SINTEF Ocean AS.

Strödecke, Daniel (2015) *Low- and high-pressure dual-fuel Technology Evaluation Process; Case Studies for LNG Carriers and Merchant Vessel*. WinGD low-speed Engines Licensees Conference.

United Nations (2022) *Review of Maritime Transport 2017*. Available at: https://unctad.org/webflyer/review-maritime-transport-2017 (Accessed: 2nd Aug. 2022).

Vestreng, V., Myhre, G., Fagerli, H., Reis, S. and Tarrasón, L. (2007) Twenty-five years of continuous sulphur dioxide emission reduction in Europe, *Atmospheric Chemistry and Physics*, 7(13), pp. 3663–3681. DOI: 10.5194/acp-7-3663-2007. Available at: https://acp.copernicus.org/articles/7/3663/2007/.

Wärtsila (2022). Available at: https://www.wartsila.com/encyclopedia/term/boil-off-gas-(bog) (Accessed: 23rd May 2022).

White, T.R. and Milton, B.E. (2008) Shock wave calibration of under-expanded natural gas fuel jets. *Springer-Verlag*, p. 116102. DOI: 10.1007/s00193-008-0158-6.

Woodyard, Doug (2004) *Pounder's Marine Diesel Engines and Gas Turbines*. 8th ed. Oxford: Elsevier Ltd.

Yau, P. S., Lee, Shuncheng, Cheng, Y., Huang, Y., Lai, S. C. and Xu, X. H. (Apr. 2013) Contribution of ship emissions to the fine particulate in the community near an international port in Hong Kong, English. *Journal de Recherches Atmospheriques*, 124, pp. 61–72. ISSN: 0169-8095. DOI: 10.1016/j.atmosres.2012.12.009.

Yu, J., Vuorinen, V., Kaario, O., Sarjovaara, T. and Larmi, Martti (2013) Characteristics of High Pressure Jets for Direct Injection Gas Engine, *Fuels and lubrication*, 6(1). DOI: 10.4271/2013-01-1619.

Zucrow, Maurice J. and Hoffman, Joe D. (1976) *Gas Dynamics*. Vol. 1. New York: John Wiley & Sons, Inc.

Appendix A

Injector Design

A.1 Technical Drawing of Injector

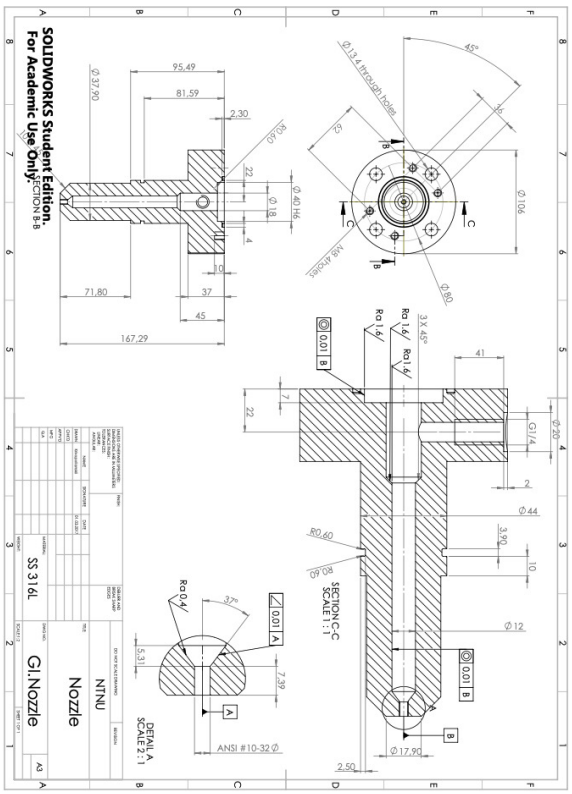

Figure A.1

A.2 Technical Drawing of Needle

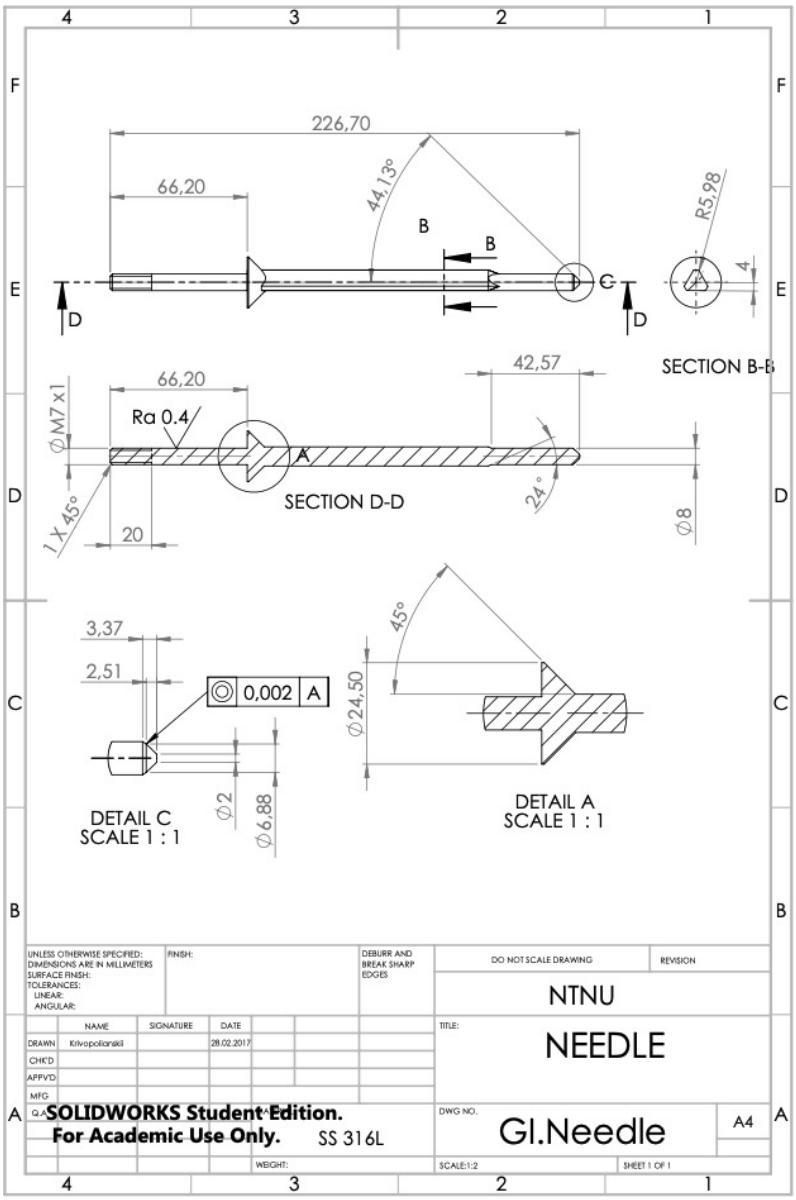

Figure A.2

Appendix B

Complementary Results

B.1 Pressure curves

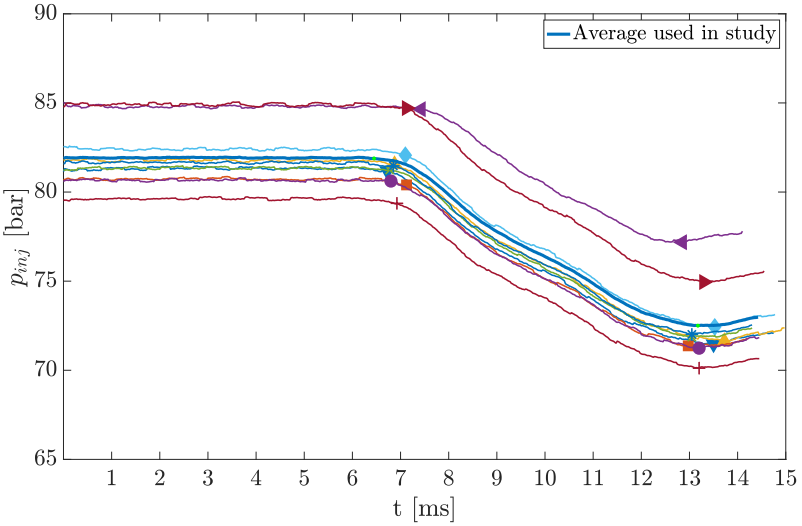

Figure B.1: Pressure curves for $p_{inj} \approx 80$

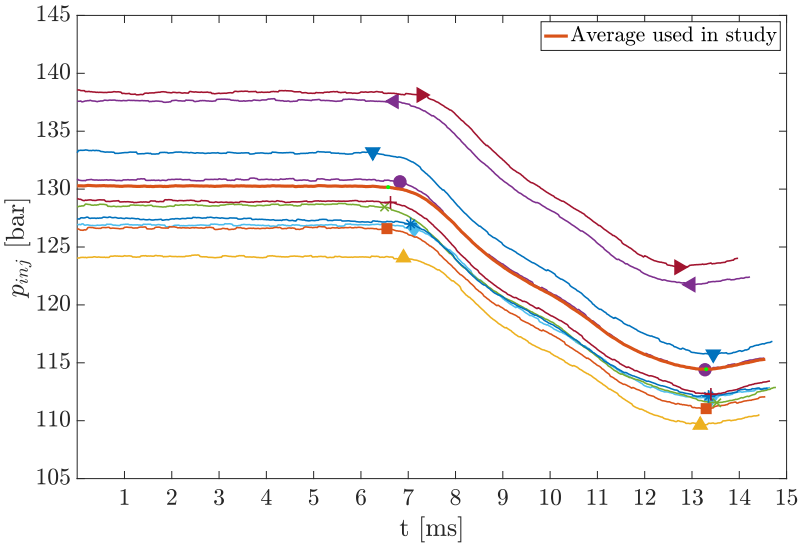

Figure B.2

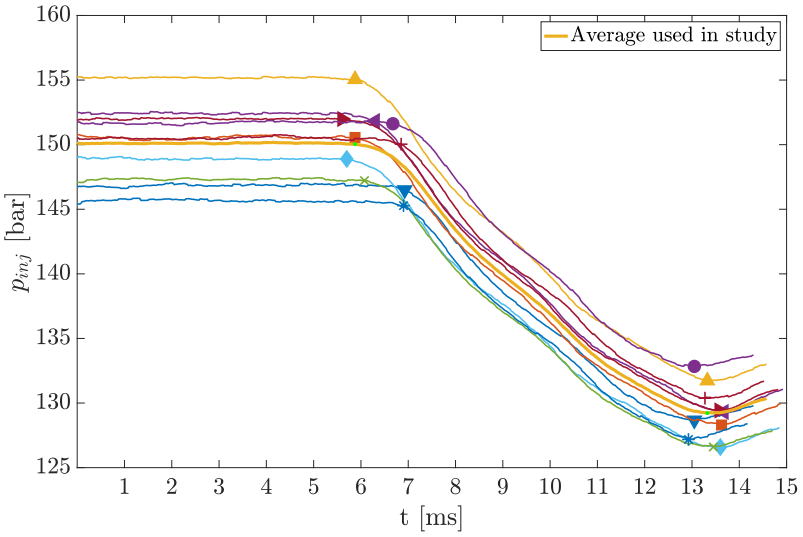

Figure B.3: Pressure curves for $p_{inj} \approx 130$

B.2 Back Pressure

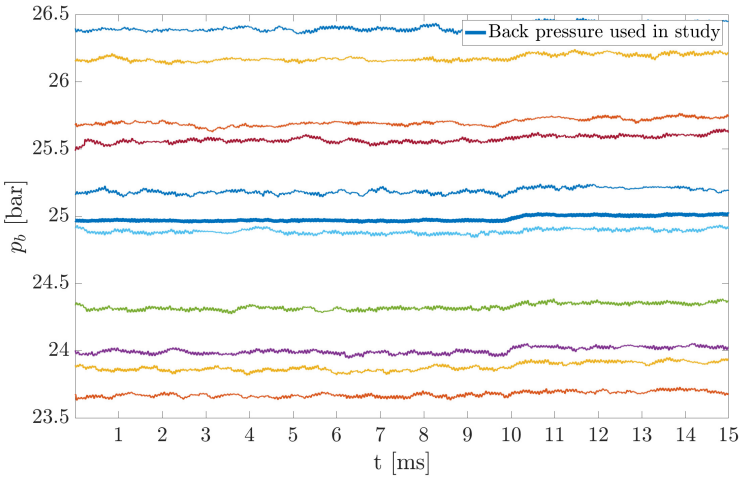

Figure B.4: Back pressure for $p_{inj} \approx 80$

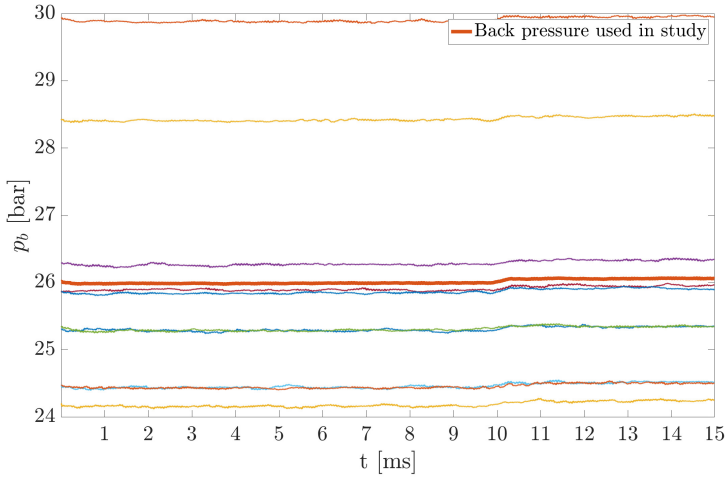

Figure B.5: Back pressure for $p_{inj} \approx 130$

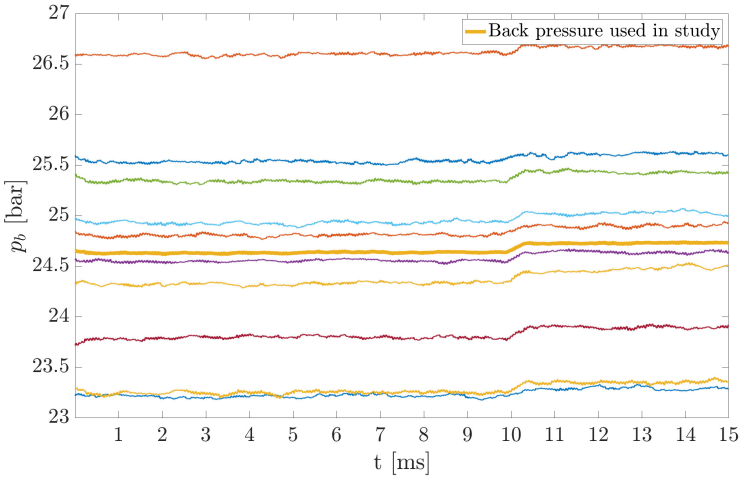

Figure B.6: Back pressure for $p_{inj} \approx 150$

B.3 Cone Angle

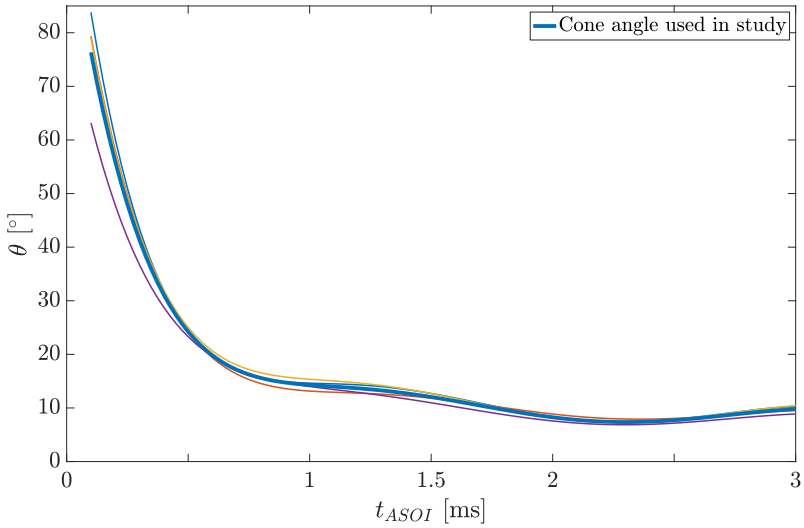

Figure B.7: Cone angles for $p_{inj} \approx 80$ bar

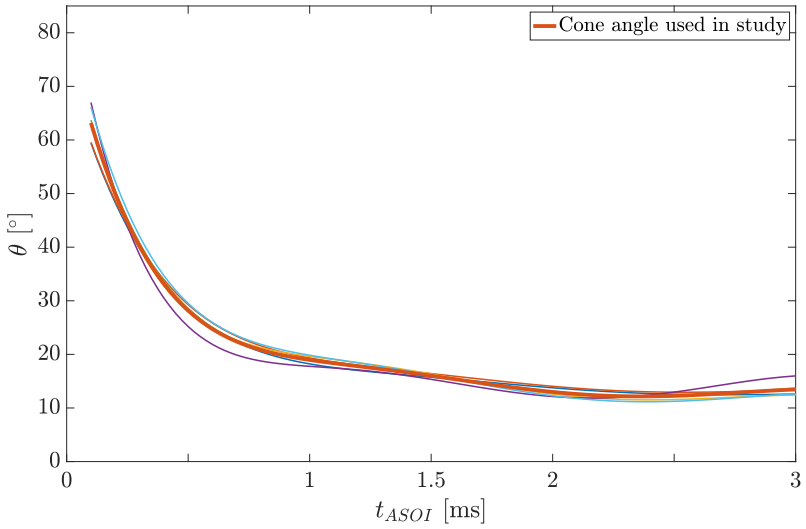

Figure B.8: Cone angles for $p_{inj} \approx 130$ bar

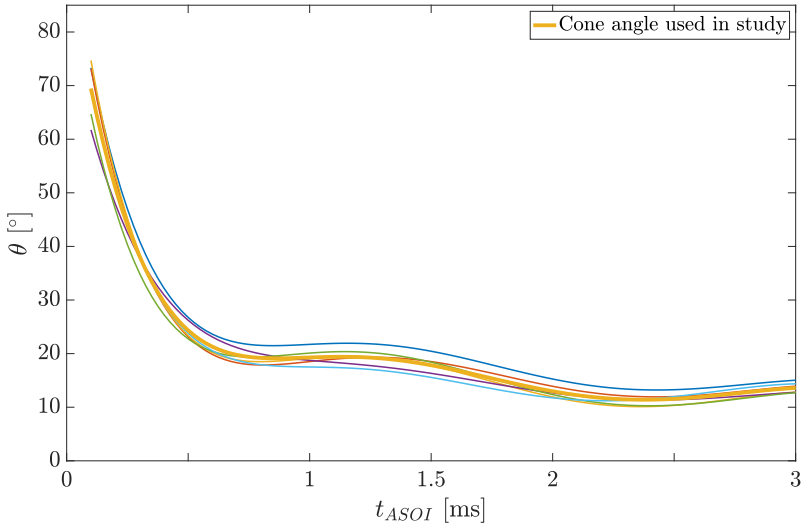

Figure B.9: Cone angles for $p_{inj} \approx 150$ bar

B.4 Penetration Length

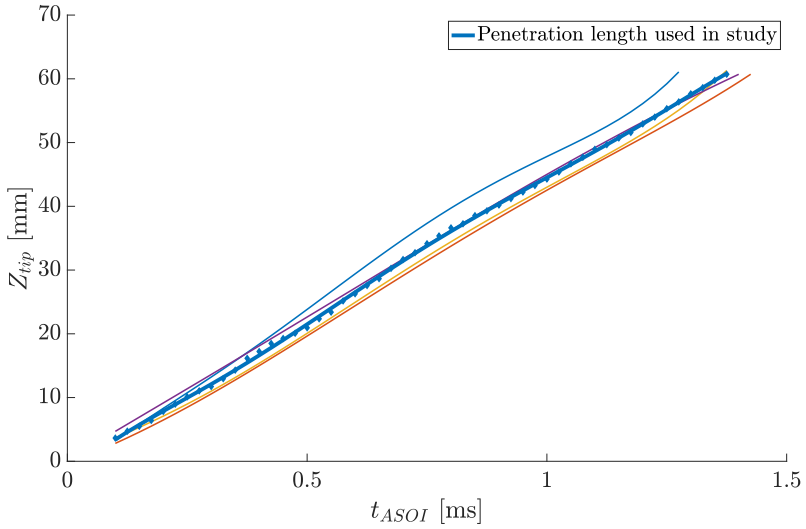

Figure B.10: Penetration lengths for $p_{inj} \approx 80$ bar

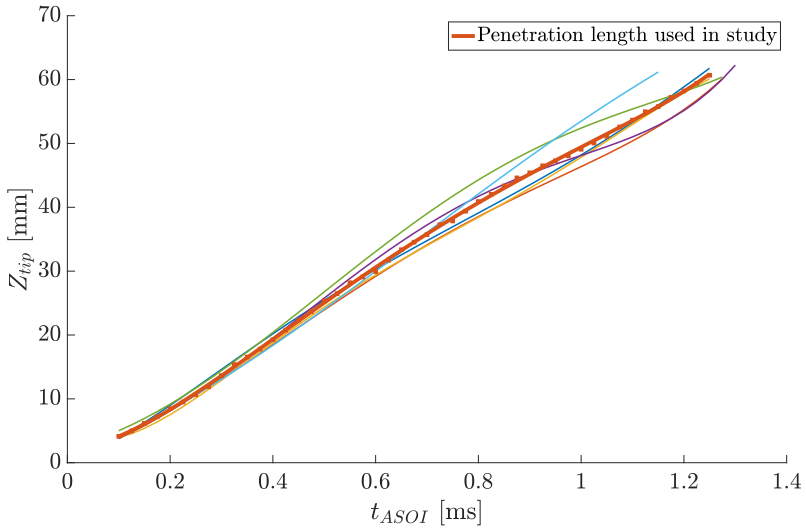

Figure B.11: Penetration lengths for $p_{inj} \approx 130$ bar

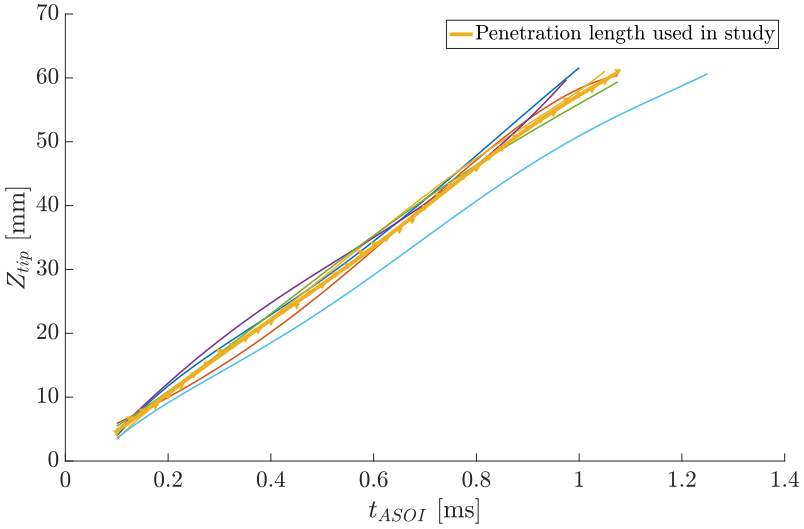

Figure B.12: Penetration lengths for $p_{inj} \approx 150$ bar

B.5 Jet Tip Velocity

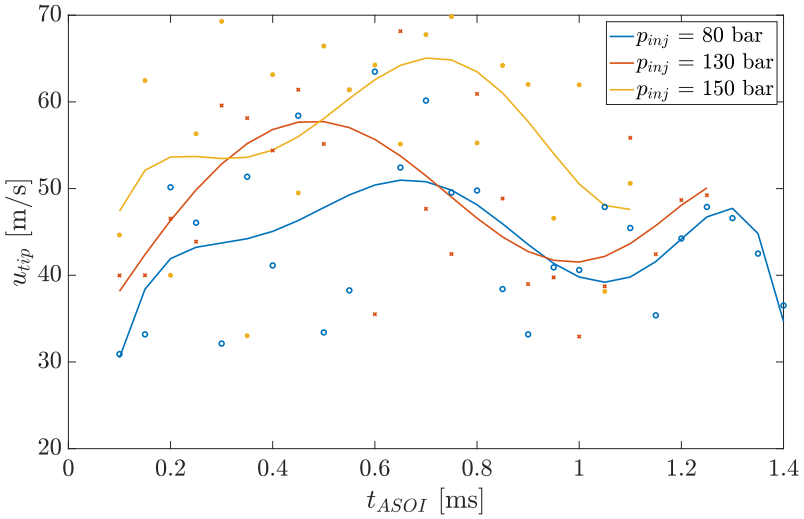

Figure B.13: Jet tip velocity with small time step

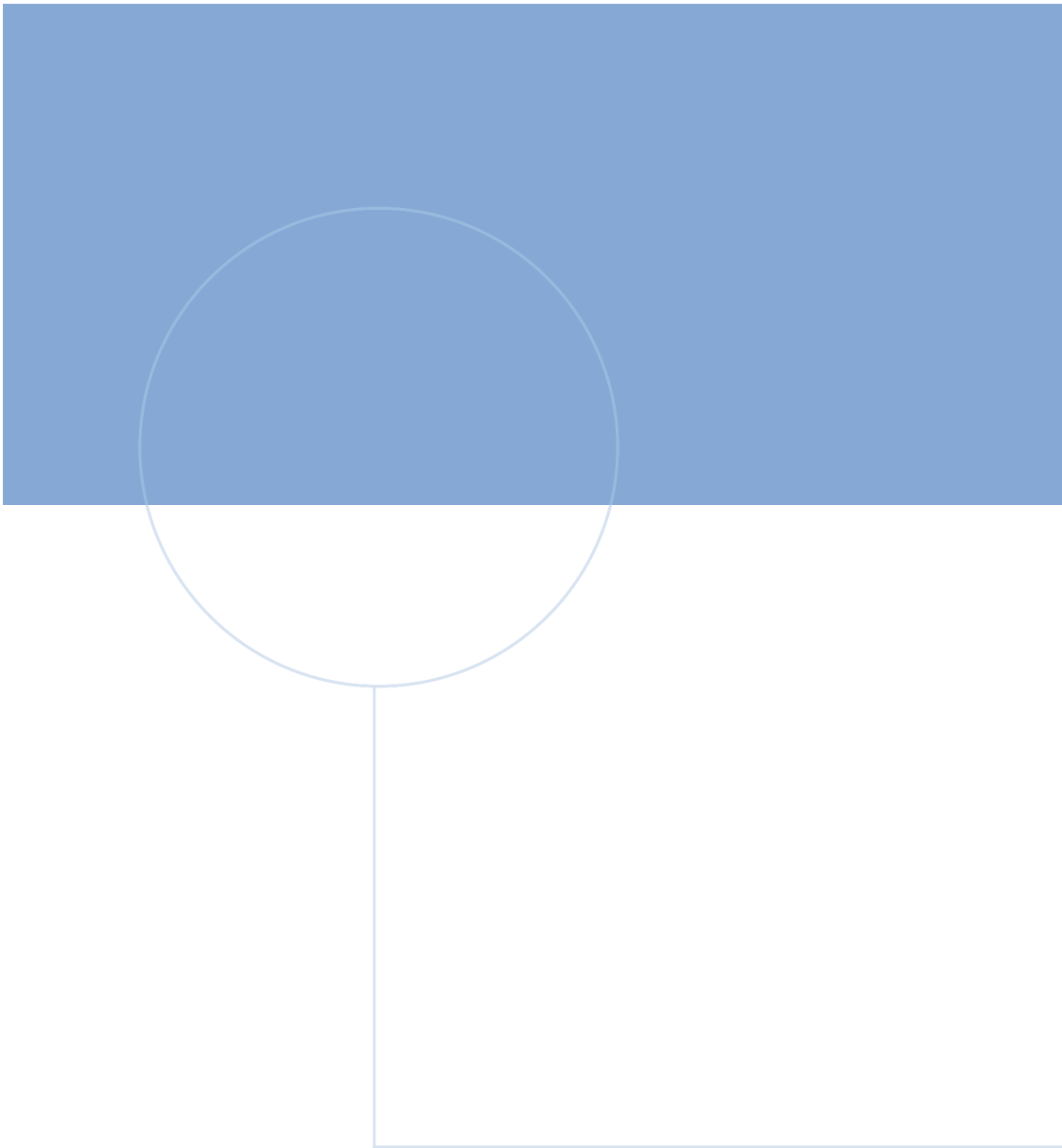

NTNU

Norwegian University of
Science and Technology